Analyzing the deformation of the left ventricle of the heart with a parametric deformable model

Eric BARDINET[1], Laurent D. COHEN[2], Nicholas AYACHE[1]

[1] INRIA Sophia Antipolis, 2004 Route des Lucioles, B.P. 93

06902 Sophia Antipolis CEDEX, France.

[2] CEREMADE, U.R.A. CNRS 749, Université Paris IX - Dauphine

Place du Marechal de Lattre de Tassigny 75775 Paris CEDEX, France.

Email: bard@sophia.inria.fr

Abstract

We present a new approach to analyze the deformation of the left ventricle of the heart, based on a parametric model that gives a compact representation of a set of points in a 3D image. We present four different approaches to tracking surfaces in a sequence of 3D cardiac images. Following tracking, we then infer quantitative parameters which are useful for the physician, such as the variation of volume and wall thickness during a cardiac cycle, the ejection fraction or the twist component in the deformation of the ventricle. We explicit the computation of these parameters using our model. Experimental results are shown in time sequences of two kinds of medical images, Nuclear Medicine and X-Ray Computed Tomography (CT).

KEYWORDS: *Parametric models, Tracking, Motion, Heart left ventricle deformation, Quantitative parameters.*

1 Introduction

The analysis of cardiac deformations has given rise to a large amount of research in medical image understanding. Indeed, cardiovascular diseases are the primary cause of mortality in developed countries. Various imaging techniques [1] allow the acquisition of dynamic sequences of 3D images (**3D+T**) during a complete cardiac cycle (contraction and dilation). These images are perfectly adapted to studying the behavior of the cardiac system since they visualize how the heart wall

deforms. Processing these images opens numerous fields of applications, like the detection and analysis of pathologies.

Advanced techniques of 3D imagery, like Nuclear Medicine and X-Ray CT, provide ever increasing resolution in space and time. Consequently, the data available to the radiologist is becoming larger. However, to establish a reliable and fast diagnosis, the physician needs models that are defined by only a small number of characteristic quantities. Our parametric deformable model allows the representation of a dynamic set of points by a reasonable number of useful parameters, as we shall see below.

Since it is characteristic of the good health of the heart, the left ventricle motion and deformation has been extensively studied by medical image processing groups. Since its creation in 1989, our group has pioneered work in the use of deformable models to extract the left ventricle [5, 17, 6, 8, 19, 16, 7, 13]. Other groups have also contributed to the understanding of the complex deformation of the ventricle [4, 31, 3, 30, 36, 29].

Over the last decade, many surface reconstruction problems have been formulated as the minimization of an energy functional corresponding to a model of the surface. Using deformable models and templates, the extraction of a shape is obtained through minimization of an energy composed of an internal regularization term and an external attraction potential (data term), illustrated for example in [23, 14, 43, 26, 41, 19, 28, 45]. The use of such models is often very efficient for locating surface boundaries of organs and structures, and for the subsequent tracking of these shapes in a time sequence.

Although previous approaches based on general deformable surfaces [19, 16] give satisfying results, they involve very large linear systems to solve. This is why the parametric model presented here is more appropriate when dealing with a huge amount of data as is the case for object tracking in a sequence of 3D images. In a previous article [11], we introduced a parametric deformable model based on a superquadric fit followed by a free-form deformation (FFD). In the present article, after a brief review of the parametric model in section 2, we describe our segmentation algorithm, specific to cardiac images, in section 3. Then, in section 4 we present several approaches to track surfaces with a parametric model in a sequence of 3D images, and give experimental results for tracking the deformation of the left ventricle in different kinds of 3D medical images. In section 5, we explain how to infer, from the parametric reconstruction, quantitative parameters which are useful for the physician, like the variation of volume and wall thickness during a cardiac cycle, the ejection

fraction or the twist component in the deformation of the ventricle.

2   A parametric model to fit 3D structures

In this section, we describe briefly the deformable model that we use to represent the inner and outer walls of the left ventricle.

We assume that a segmentation algorithm has already been applied to the 3D images of the heart to extract a number of 3D points belonging to the surface of the inner or outer wall of the left ventricle (this algorithm is described in section 3).

The advantage of parametric deformable templates such as superquadrics or hyperquadrics is the small number of parameters needed to represent a shape. However, if these models give a good global approximation to a surface, the set of shapes described by superquadrics is too limited to approximate precisely complex surfaces. To take into account local deformations, Terzopoulos and Metaxas [42] couple superquadrics with a deformable model. In [15], an implicit approach is used to refine the initial approximation.

We refine our superquadric model using a parametric deformation. More precisely, for a given set of 3D points, we first fit 3D data with a superellipsoid, and then refine this crude approximation using Free Form Deformations (FFDs).

2.1   Fitting 3D data with superquadrics

Superquadric shapes have been widely used in Vision and Graphics. In computer vision, their first use is due to Pentland [32], followed by Solina and Bajcsy [9, 37, 38] who used superellipsoids to approximate 3D objects. The goal of the algorithm is to find a set of parameters such that the superellipsoid best fits the set of data points. Superquadrics form a family of implicit surfaces obtained by extension of conventional quadrics. Superellipsoids are defined by the implicit equation:

$$\left(\left(\left(\frac{x}{a_1} \right)^{2/\epsilon_2} + \left(\frac{y}{a_2} \right)^{2/\epsilon_2} \right)^{\epsilon_2/\epsilon_1} + \left(\frac{z}{a_3} \right)^{2/\epsilon_1} \right)^{\epsilon_1/2} = 1. \tag{1}$$

Suppose that the data we want to fit with the superellipsoid are a set of 3D points $(x_i, y_i, z_i), i = 1, \cdots, N$. Since a point on the surface of the superellipsoid satisfies $F = 1$, where F is the function defined by equation (1), we find the minimum of the following energy:

$$E(A) = \sum_{i=1}^{N} \left[1 - F(x_d, y_d, z_d, a_1, a_2, a_3, \epsilon_1, \epsilon_2) \right]^2, \tag{2}$$

using a minimization algorithm (see [10] for details and also for a geometric interpretation of this energy).

2.2 Refinement with Free Form Deformations (FFDs)

We now refine this parametric representation of the 3D data, using a global volumetric deformation called FFD. This is a tool devoted to the deformation of solid geometric models in a free-form manner (see [33]). The main interest of FFDs is that the resulting deformation of the object, although potentially complex, is defined by a small number of points. This characteristic feature allows us to represent voluminous 3D data by a model defined by a small number of parameters.

2.2.1 Definition of FFDs

FFDs were introduced by Sederberg and Parry [33] in computer graphics and have been used to solve matching problems by Szeliski and Lavallée [39, 40]. An FFD is a mapping from $\mathbb{R}^3$ to $\mathbb{R}^3$, defined by the tensor product of trivariate Bernstein polynomials. The principle of FFDs is as follows: the object to be deformed is embedded in a 3D box. Inside this box, a volumetric grid of points is defined, which links the box to the object (by the trivariate polynomial which defines the deformation function). This can be written in a matrix form: $\boldsymbol{X} = \boldsymbol{BP}$, where $\boldsymbol{B}$ is the deformation matrix $ND \times NP$ (ND is the number of points on the discretized superellipsoid and NP is the number of control points of the grid), $\boldsymbol{P}$ is a matrix $NP \times 3$ which contains coordinates of the control points and $\boldsymbol{X}$ is a matrix $ND \times 3$ with coordinates of the model points. The box is then deformed by the displacement of its lattice, and the position of a point of the deformed object is computed (see [11] for details).

2.2.2 The inverse problem

We need to solve the inverse problem: first compute a displacement field $\delta\boldsymbol{X}$ between the superellipsoid and the data, and then, after having put the superellipsoid in a 3D box, search for the deformation $\delta\boldsymbol{P}$ of this box which will best minimize the displacement field $\delta\boldsymbol{X}$:

$$\min_{\delta\boldsymbol{P}} \|\boldsymbol{B}\delta\boldsymbol{P} - \delta\boldsymbol{X}\|^2 \tag{3}$$
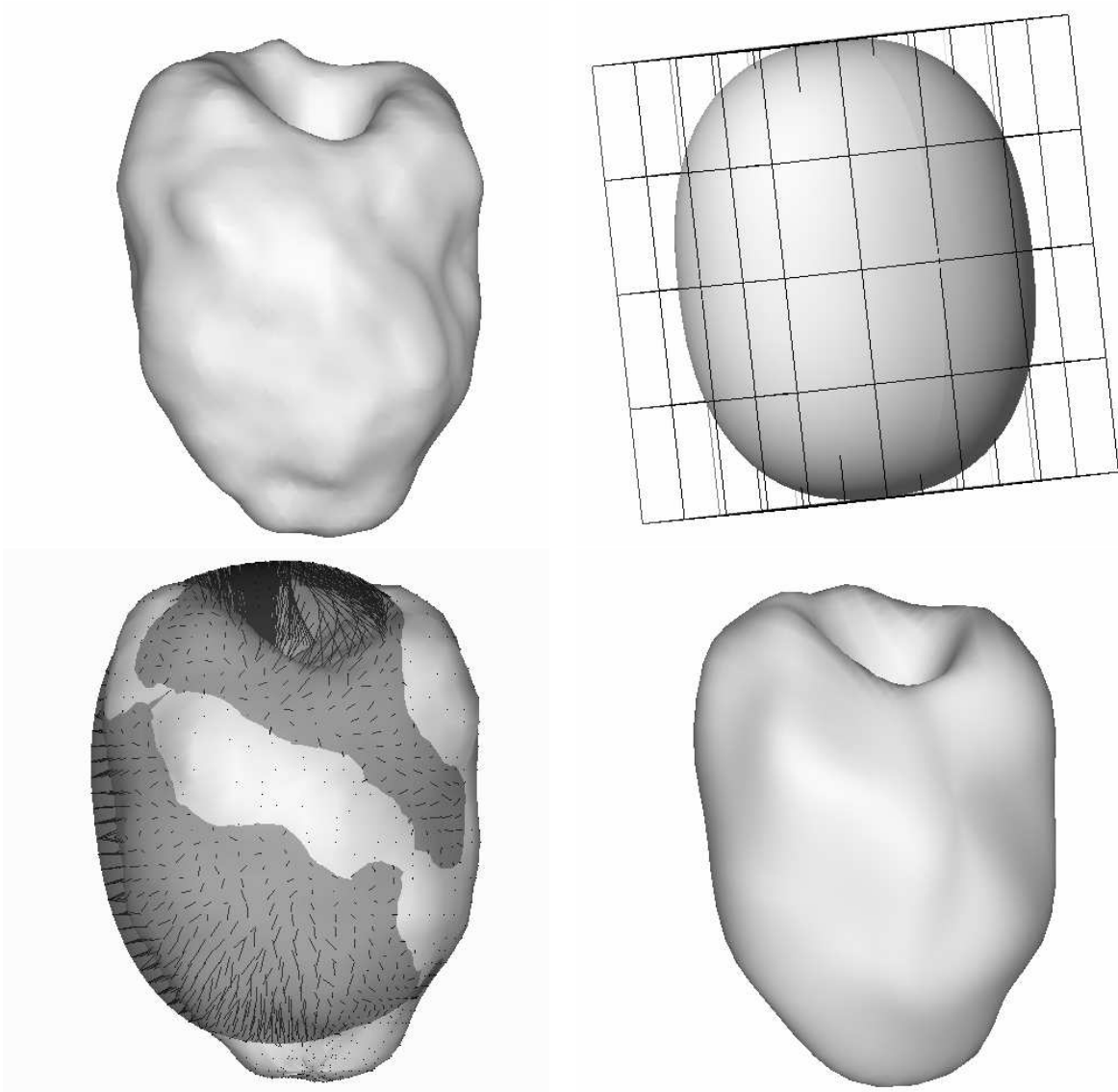
This is illustrated in figure 1.

Figure 1: From the superellipsoid to the final model. Top left: data. Top right: superellipsoid fit and initial box of control points. Bottom left: displacement field between data and the superellipsoid. Bottom right: final model after minimization of the displacement field (see [11] for details).

2.2.3 Iterative algorithm

To represent 3D data with our model, we use an iterative two-step algorithm:

Step 1 : Computation of the displacement field between the previous estimation $\boldsymbol{X}_n$ and its projection on data $\boldsymbol{X}_n^a$, $\delta\boldsymbol{X}_n$ such as: $\boldsymbol{X}_n^a = \boldsymbol{X}_n + \delta\boldsymbol{X}_n$

Step 2 : Computation of the control points $\boldsymbol{P}_{n+1}$ by minimization of $\|\boldsymbol{BP} - \boldsymbol{X}_n^a\|^2$

Computation of the deformed model: $\boldsymbol{X}_{n+1} = \boldsymbol{BP}_{n+1}$

Stop test on the least-squares error $\|\boldsymbol{X}_{n+1} - \boldsymbol{X}_n\|$

$\boldsymbol{P}_0$ is defined as a uniformly spaced parallelepiped box of control points and $\boldsymbol{X}_0 = \boldsymbol{BP}_0$ represents the set of points of the initial discretized superellipsoid. This algorithm is similar to the formulation of the B-splines snakes with auxiliary variables, as described in [18].

Size of the FFD	Computation time
$2 \times 2 \times 2 = 8$	243
$3 \times 3 \times 3 = 27$	244
$4 \times 4 \times 4 = 64$	265
$5 \times 5 \times 5 = 125$	429
$6 \times 6 \times 6 = 216$	751

Table 1: Typical computation times (in seconds) with an increasing number of control points of the FFD for 20 iterations.

In practice, we use boxes of size $5 \times 5 \times 5$ for data composed of about 6,000 points, and the number of iterations is between 10 and 30. Therefore we get a compression rate of 47 (computed as $(6000 \times 3)/(125 \times 3 + 11)$, where 11 corresponds to the parameters needed for the superellipsoid. In the following, we will write that the model is defined by 130 points). Table 1 presents typical computation times of the FFD with 20 iterations and different sizes for the box of control points (on a DEC Alpha 300). One can get a qualitative idea of the algorithmic complexity from figure 2.
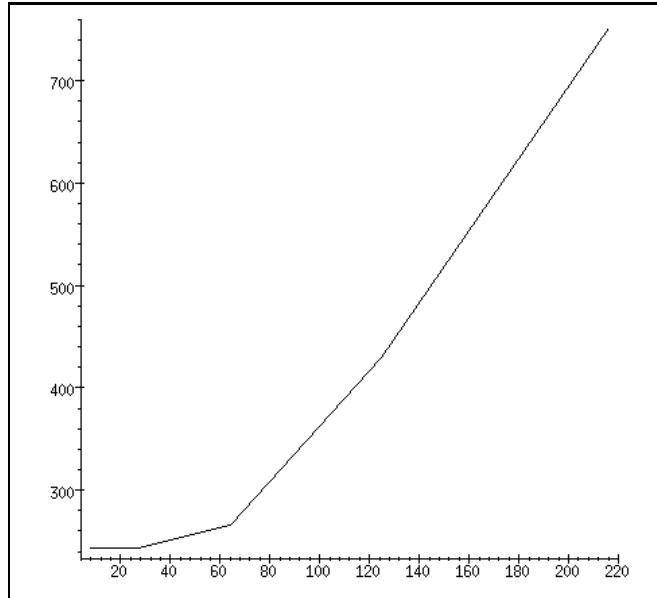
2.2.4 Simultaneous deformation of two surfaces

Figure 2: Computation time vs. number of control points (number of columns of the matrix B).

An essential feature of this algorithm is that FFD is a volumetric deformation. This means that several objects can be deformed simultaneously with only one FFD. Using only one model means that the two surfaces are put in a same box of control points, and the minimization of equation (3) is done simultaneously on the union of both displacement fields. This shows that our model can handle the deformation of many connected components at the same time by merging the respective displacement constraints. This presents no difficulty since we have a 3D box which defines a really 3D deformation. Moreover, our model gives an interpolation of the 3D deformation everywhere in the volume between the two surfaces. Figure 3 shows the result of the algorithm for the reconstruction of the epicardium and the endocardium, first with one FFD for each surface, and then simultaneously computed with only one FFD (the fact that the two surfaces intersect each other at the top and may cause some artefacts for the rendering is not important as will be explained in Section 3.3). In this last case, the unique box of control points is the one previously computed for the epicardium, thus including the two surfaces. The corresponding approximation errors are presented in table 2. One can see that using two FFDs for the two surfaces leads to a better quality of approximation. On the other hand, using only one FFD allows to reduce the number of parameters by half, yielding a larger compression of the information needed for the description of the parametric model. It also permits to infer from this single FFD, a deformation
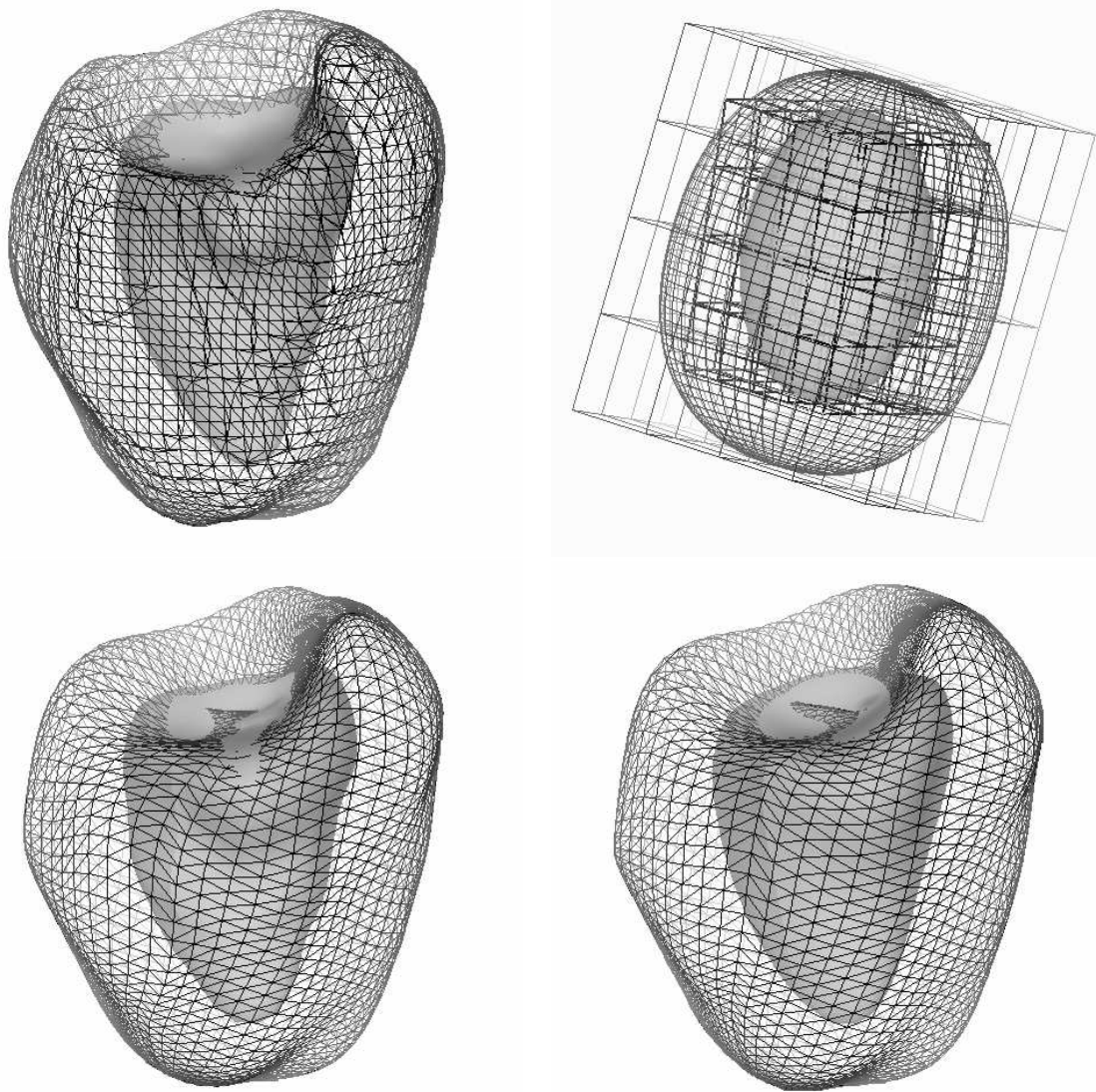
Figure 3: Deformation of two surfaces. Top left: data: epicardium (mesh) and endocardium (rendered surface) described respectively with 4500 and 1500 points. Top right: two fitted superellipsoids and the two initial boxes of control points. Bottom left: final models obtained with two FFDs (each defined by 130 points). Compression ratio: 23. Bottom right: simultaneous deformation of the two superellipsoids with only one FFD (defined by 130 points). Compression ratio: 46.

	Separate computation	Simultaneous computation	Precision lost
Epicardium	0.007448	0.008236	10.5 %
Endocardium	0.012838	0.014376	11.9 %

Table 2: Least-square errors $\|\boldsymbol{BP} - \boldsymbol{X}\|$ between original data and parametric models. Left column: each model is computed independently. Middle column: the two models are computed with one FFD. Right column: computation with only one FFD leads to a slight loss of the approximation precision.

field over the entire space, due to the volumetric formulation of FFDs. In the particular case of cardiac deformations, it allows estimation of the deformation at any point within the volume between the epicardium and the endocardium, namely the myocardium. We show in figure 4 the
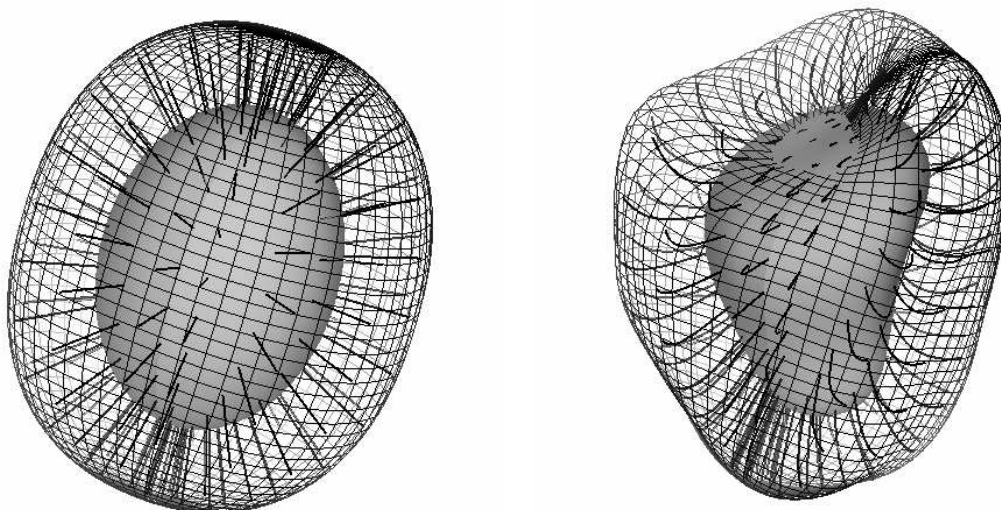

Figure 4: Volumetric deformation. FFD previously computed simultaneously from the two isosurfaces (figure 3) is applied to rigid links between the two superellipsoid models (on the left) and provides an elastic volumetric deformation of the myocardium (on the right).

effect of the FFD applied to the volume between the two superellipsoids. To visualize this volume information, we show on the left the segments linking these two surfaces. The FFD computed to obtain simultaneously the epicardium and the endocardium surfaces also deforms these segments.

3 Segmentation of cardiac images

In order to get sets of 3D points which correspond to the anatomical structure that we want to track (epicardium and endocardium of the cardiac left ventricle), and therefore fit our model on these sets of points, we have to segment the original data.

The models were computed on two different kinds of images:

- Nuclear medicine data, the SPECT sequence, with 8 successive time frames during one cardiac cycle. Each image is a volume of $64 \times 64 \times 64$ voxels.

- X-Ray CT data, the DSR sequence, with 18 successive time frames during one cycle. Each image is a volume of $98 \times 100 \times 110$ voxels (size of the voxel: 0.926 mm^3).

The original 3D images are visualized as a series of 2D cross-sections (transverse slices) in figures 5 and 6. On the DSR data, the ventricular cavity (high grey levels) is clearly shown up but the outer wall of this cavity does not stand out, thus we will use the DSR sequence to analyze the deformation of the inner wall of the left ventricle (endocardium). On the SPECT sequence, which is with high contrast, we will study at the same time the deformation of the inner and outer walls of the left ventricle (endocardium and epicardium). As one can observe from figures 5 and 6, the extraction of the endocardium on the DSR image is not a very difficult task, because of the high contrast between the endocardium and the rest of the image. Concerning the SPECT images, which are also fairly noisy, a single thresholding will not provide the areas of interest.

We first recall some properties of SPECT and DSR techniques (sections 3.1 and 3.2) and then detail our specific segmentation algorithm in section 3.3.

3.1 Nuclear medicine data (SPECT)

Nuclear Medicine provides two types of images: 1. PET (Positron Emission Tomography) and 2. SPECT (Single Photon Emission Computed Tomography). These medical imaging modalities constitute the two different modalities of ECT (Emission-Computed Tomography). ECT has been widely used in biomedical research and clinical medicine during the last twenty years. ECT differs fundamentaly from many other medical imaging modalities in that it produces a mapping of physiological functions as opposed to visualizing anatomical structure. SPECT imaging techniques employ radioisotopes which decay emitting a single gamma photon. This represents the fundamental difference between SPECT and PET. A typical transaxial resolution in SPECT ranges from
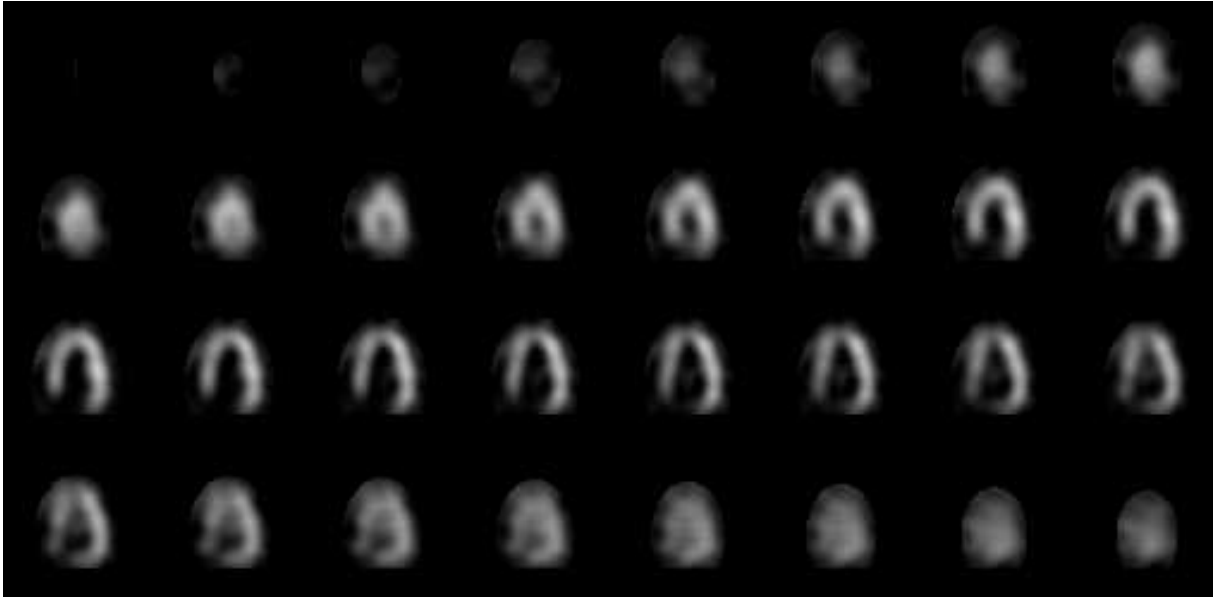
Figure 5: 3D image of the left ventricle - SPECT image (the order of sections reads from left to right and from top to bottom and descends through the heart).

10 to 20 mm. Resolution in the axial direction specifies the slice thickness and is determined by the collimation properties of the detectors; typically the axial resolution ranges from 10 to 20mm. One can find a complete description of the Nuclear Medicine imaging techniques in the tutorial article [1].

3.2   X-Ray CT data (DSR)

The images of this time sequence have a very high resolution ($98 \times 100 \times 110$ for a voxel size of 0.926 mm^3). They were obtained with the Dynamic Spatial Reconstructor (DSR), which is a X-Ray CT Scanner capable of providing dynamic synchronous volume 3D CT images, with a time step of $1/60$ s. X-Ray CT is a medical imaging modality which allows acquisition of a 3D representation of internal anatomical structures. A complete description of X-Ray imaging techniques can also be found in the tutorial article [1]. To get these images, a contrast agent has been injected into the ventricle, enhancing the appearance of the cavity.

Figure 6: 3D image of the left ventricle - DSR image (the order of sections reads from left to right and from top to bottom and descends through the heart).

3.3   Morphological segmentation

To obtain an accurate and robust segmentation, we must combine thresholding with mathematical morphology and connected components analysis (as in Hoehne [25]). We first choose a threshold which grossly separates the ventricle (high values in SPECT and DSR images) from the rest of the image. The same value is chosen for the whole sequence of images, which makes the algorithm entirely automatic. Then we choose the largest connected component for each of the resulting 3D binary images, and perform a morphological closing of order k (a closing of order k consists in a series of k dilations followed by the same number of erosions [34, 35]). Typically, this number is equal to 3. This last operation is necessary to bridge small gaps and smooth the overall segmentation. Finally, the extraction of the isosurfaces from this sequence of images provides the set of 3D points that we need as input for the following reconstruction and tracking algorithm. However, it has to be precised that this set is unstructured. This is why getting a representation as we give is an important contribution.

To understand the complex behavior of the cardiac muscle, we have to recover the deformations of both the internal and external walls of the myocardium, namely the endocardium and the epicardium. It is possible to represent the geometry of the complete myocardium by a single deformable superellipsoid-based model. However, by recovering the large concavity which corresponds to the ventricular cavity, which means a strong displacement constraint, it follows that all the other constraints are neglicted, thus involving a smoothing effect on the surface model. On the other hand, the shape of the myocardium looks very much like two deformed concentric ellipsoids, and it is thus natural to use two models to recover the two cardiac walls.

As we said, the segmentation of the SPECT sequence provides a set of isosurfaces. To get two separate closed surfaces of the epicardium and endocardium, we use again morphological operations (closings and logic additions). For this reason, we have artificial caps at the base of the heart (on top of the figures, for example in figures 11 and 12). This yields to some slight visual artifacts, because the two surfaces intersect each other at the top, but this effect is minor both on the following computation of quantitative parameters (cf. section 5) or for the qualitative analysis which is based mainly on the observation of the remaining part of the surface.

Results of those operations on the dynamic sequence are presented on figures 11 and 13 (one cross-section over time). For a correct estimation of the quality of those segmentations, we superimposed the segmented surface on the image.

Although extracting isosurfaces from the SPECT sequence seems to be a fiddly task, it is made totally automatic. First, an initial threshold is used to isolate the myocardium. The threshold is set at 40% of the histogram maximum, similarly to the procedure developed by Pr. Michael Goris at Stanford for the analysis of SPECT images [22]. From this thresholded image, we obtain an isosurface which represents the myocardium. It has two components, as seen on figure 11. To get the two isosurfaces corresponding to the walls of the myocardium, we first apply a morphological closing which provides the external surface (epicardium), and then, by application of a mask, we erase the external surface from the myocardium isosurface and get the internal surface (endocardium).

4 Dynamic tracking of the left ventricle

Having extracted 3D points corresponding to the walls of the left ventricle in a time sequence of images, we show in this section how we use our parametric model of section 2 to make an efficient tracking of the LV wall in a sequence of 3D images of different modalities.

We present four strategies to use this model to track surfaces in a sequence of 3D images in section 4.1. To make an efficient comparison between those strategies, we present in this section error measurements and results computed on a synthetic example: a sequence of parametric surfaces representing a synthetic heart during a complete cardiac cycle (17 successive time frames), see figure 7. All the hearts of this sequence were obtained with the following implicit equation:

$$\left(\left(\frac{x}{a_1}\right)^2 + \left(\frac{y}{a_2}\right)^2 + \left(\frac{z}{a_3}\right)^2\right)^3 - \left(c_1\left(\frac{x}{a_1}\right)^2 + c_2\left(\frac{y}{a_2}\right)^2\right)\left(\frac{z}{a_3}\right)^3 = 1,$$

with different values for c_1 and c_2. Actually, a synthetic example is well suited to compare the theoritical pros and cons of each strategy, and to choose the most accurate one for the analysis of cardiac motion.

We then present examples on two sequences of 3D medical images in section 4.2. In the following chapter, we will show how to take advantage of the parametric model to easily compute some important quantitative parameters which help to characterize cardiac motion, in particular the variation of volume and wall thickness during a cardiac cycle, the ejection fraction or the twist component.
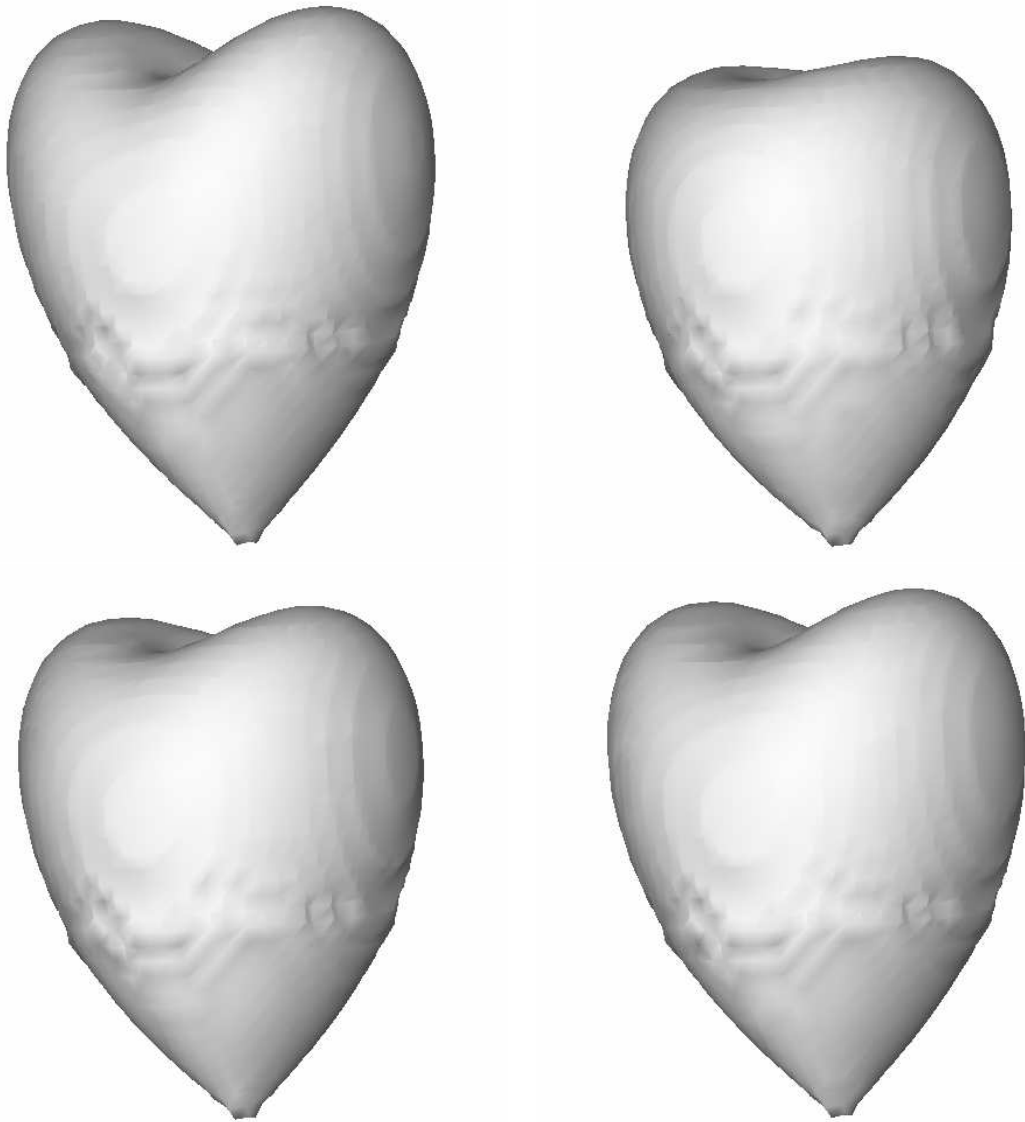
Figure 7: Synthetic beating heart (17 successive time frames). From top to bottom and from left to right: frame 1, 8, 12, 15.

4.1 Four tracking strategies

Generally deformable models need an initialization which is close enough to the solution. This is convenient for tracking in medical images since the deformation between two images is small and the model can start with the solution in the previous image as an initialization for the current one.

Deformable contours have been used for tracking boundaries since their introduction by Kass, Witkin and Terzopoulos [43]. This was applied to spatial tracking of the ventricle boundary in successive cross-sections of a 3D MR image in [17], in view of 3D reconstruction from a sequence of 2D models, and later applied to temporal tracking for ultrasound images in [8].

With our parametric deformable model, the initialization is made automatically through the initial superquadric fit (see section 2.1), and then refined by the FFD. We studied four different approaches for tracking which are described in figure 8 and now briefly presented. We computed for each strategy a global error ($\|\boldsymbol{BP} - \boldsymbol{X}\|$), which consists in projecting each 3D data point onto the deformed model (see figure 9).

4.1.1 Fitting the model independently to each image

This first approach consists in fitting the deformable model independently to each segmented 3D image. In this approach, we do not use the continuity of the motion, and the deformation obtained at time n does not take advantage of the deformation computed at time $n - 1$. The error curve labelled 1 in figure 9 show the global errors between the model and the 3D points of the synthetic sequence. This is clearly the least accurate approach to computing the volumetric properties of the ventricle. On the other hand, we do not need any previous model information to define the model at time n, but only the superellipsoid and the FFD.

Following the formulation of section 2.2.3, the model at time n, $\boldsymbol{X}_n$, can be written:

$$
\begin{cases}
\boldsymbol{X}_0^{sq} & = & \boldsymbol{B}_0 \boldsymbol{P}_0 \\
\boldsymbol{X}_0 & = & \boldsymbol{B}_0 \left(\boldsymbol{P}_0 + \delta \boldsymbol{P}_0^*\right) \\
\boldsymbol{X}_1^{sq} & = & \boldsymbol{B}_1 \boldsymbol{P}_1 \\
\boldsymbol{X}_1 & = & \boldsymbol{B}_1 \left(\boldsymbol{P}_1 + \delta \boldsymbol{P}_1^*\right) \\
& \vdots & \\
\boldsymbol{X}_n^{sq} & = & \boldsymbol{B}_n \boldsymbol{P}_n \\
\boldsymbol{X}_n & = & \boldsymbol{B}_n \left(\boldsymbol{P}_n + \delta \boldsymbol{P}_n^*\right)
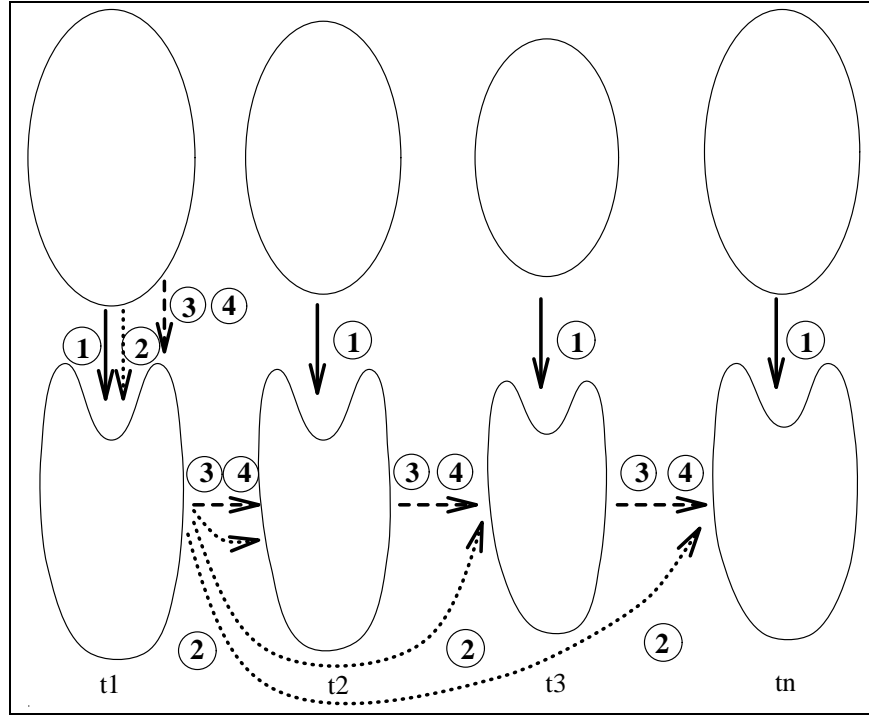\end{cases}
$$

Figure 8: Four tracking strategies to deal with a temporal sequence. 1: Fitting at each time step a superquadric and deforming it with an FFD (section 4.1.1). 2: Deforming at time step n the result obtained at time 1 by one additional FFD (section 4.1.2). 3: Deforming at time step n the result obtained at time $n-1$ by one additional FFD (section 4.1.3) 4: Deforming at time step n a superquadric with a single FFD, initialized from the FFD obtained at time $n-1$ (section 4.1.4).
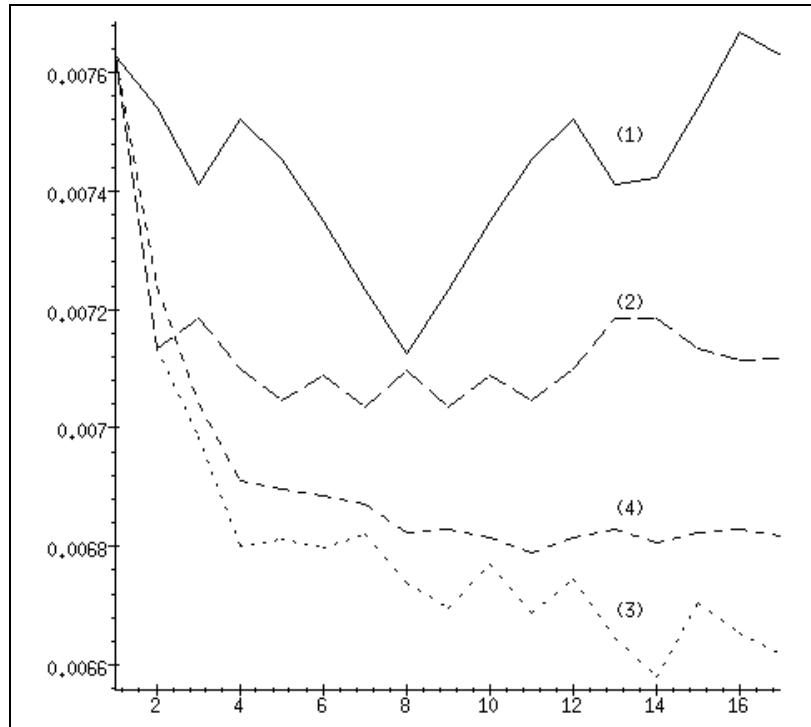
Figure 9: Four tracking strategies (2). Time evolution of the least square error between the data (synthetic sequence, see figure 7) and the final model for the 17 frames. The four curves correspond to the four approaches.

where $P_i + \delta P_i^*$ denotes the result of the minimization of $\|B_i \, P_i - X_i^a\|$ (see section 2.2.3), and X_i^{sq} denotes the sequence of initial superellipsoids.

4.1.2 Independent representation with a reference deformation

A superellipsoid is computed and deformed by a FFD to fit the surfaces extracted in the first image. This then acts as a reference surface which is deformed by only one additional FFD, to fit the surfaces extracted in image n. The error curve is shown in figure 9 by the curve labelled (2). The approximation is more accurate, being the composition of two FFDs and each image is now described with only one set of superellipsoid parameters and two FFDs. This technique is thus independent of the length of the time sequence. The method is a trade-off between the techniques of section (4.1.1) and section (4.1.3).

As with the previous method, this approach does not provide temporal processing, but the use of a reference model achieves more accurate solutions.

Following the formulation of section 2.2.3, the model at time n, X_n, can be written:

$$
\begin{cases}
X_0^{sq} & = & B_0 P_0 \\
X_0 & = & B_0 \left(P_0 + \delta P_0^* \right) \\
X_0 & = & B_1 P_1 \\
X_1 & = & B_1 \left(P_1 + \delta P_1^* \right) \\
X_1 & = & B_1 P_2 \\
& \vdots & \\
X_{n-1} & = & B_1 P_n \\
X_n & = & B_1 \left(P_n + \delta P_n^* \right)
\end{cases}
$$

where $P_i + \delta P_i^*$ denotes the result of the minimization of $\|B_1 \, P_i - X_i^a\|$ (see section 2.2.3), and X_0^{sq} denotes the initial superellipsoid at time 0.

4.1.3 Recursive representation

This approach is real temporal tracking. The complete model (superquadric fitting and free-form-deformation) is applied only to the data of the first image. Then, at time n, the model is obtained from the previous one by deforming the shape obtained at time $n-1$ by a new FFD. Therefore, the surface at time n is obtained from the superellipsoid at time 1 iteratively deformed by a sequence of n successive FFDs. This provides the advantage of being an increasingly accurate approximation,

but at the expense of a number of parameters increasing linearly with the number of images (the model at time n is defined by n FFDs). The error curve is shown in figure 9 by the curve labelled (3).

Following the formulation of section 2.2.3, the model at time n, $\boldsymbol{X}_n$, can be written:

$$
\left\{
\begin{aligned}
\boldsymbol{X}_0^{sq} &= \boldsymbol{B}_0 \boldsymbol{P}_0 \\
\boldsymbol{X}_0 &= \boldsymbol{B}_0 \left(\boldsymbol{P}_0 + \delta \boldsymbol{P}_0^* \right) \\
\boldsymbol{X}_0 &= \boldsymbol{B}_1 \boldsymbol{P}_1 \\
\boldsymbol{X}_1 &= \boldsymbol{B}_1 \left(\boldsymbol{P}_1 + \delta \boldsymbol{P}_1^* \right) \\
\boldsymbol{X}_1 &= \boldsymbol{B}_2 \boldsymbol{P}_2 \\
&\vdots \\
\boldsymbol{X}_{n-1} &= \boldsymbol{B}_n \boldsymbol{P}_n \\
\boldsymbol{X}_n &= \boldsymbol{B}_n \left(\boldsymbol{P}_n + \delta \boldsymbol{P}_n^* \right)
\end{aligned}
\right.
$$

where $\boldsymbol{P}_i + \delta \boldsymbol{P}_i^*$ denotes the result of the minimization of $\| \boldsymbol{B}_i \, \boldsymbol{P}_i - \boldsymbol{X}_i^a \|$.

4.1.4 Recursive representation with a unique deformation

This approach is also real temporal tracking. The difference with the previous method is that only one FFD is needed to compute all the parametric models in the sequence. More precisely, the complete model is fitted only to the data of the first image. Then, a unique FFD (which is now a deformed box of control points) is used with a new displacement field computed between the previous model and the data of the next image, and so on for the complete sequence. Finally, the models at any time are defined by only one FFD applied to a single original superellipsoid. The error curve is shown in figure 9 by the curve labelled (4).

Following the formulation of section 2.2.3, the model at time n, $\boldsymbol{X}_n$, can be written:

$$
\boldsymbol{X}_n = \boldsymbol{B}_0 \left(\boldsymbol{P}_0 + \delta \boldsymbol{P}_0^* + \cdots + \delta \boldsymbol{P}_{n-1}^* \right), \tag{4}
$$

where $\boldsymbol{P}_i + \delta \boldsymbol{P}_i^*$ denotes the result of the minimization of $\| \boldsymbol{B}_0 \, \boldsymbol{P}_i - \boldsymbol{X}_i^a \|$.

4.1.5 Discussion

From the error curve of figure 9, one can see that the second method is superior to the first one by reducing and even stabilizing the error values after time frame 2. In addition, methods 3 and 4, which provide a real temporal tracking (this is the reason why these curves are decreasing)
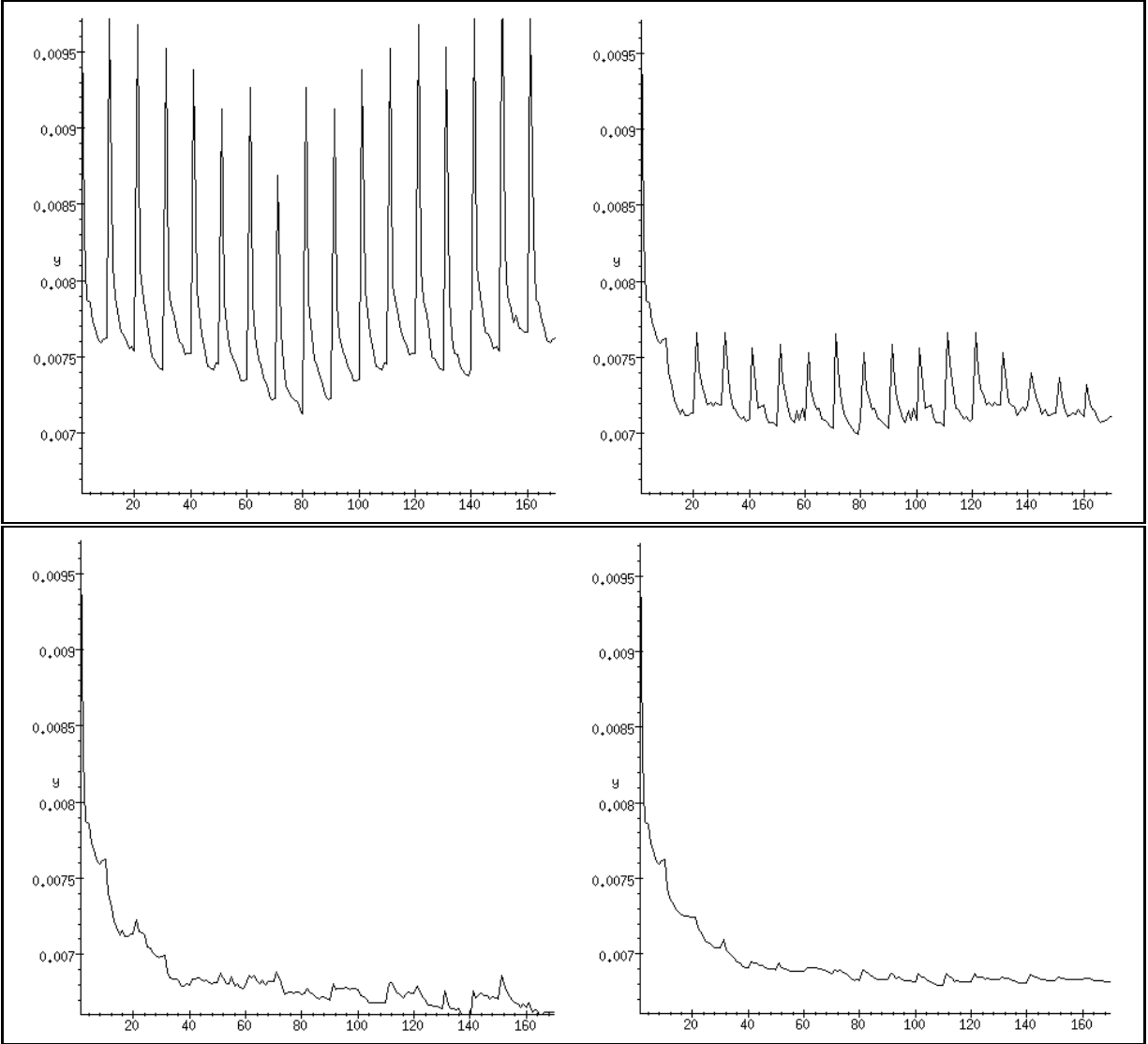
Figure 10: Four tracking strategies (4). Temporal evolution of the least square error between the data and the model during the complete sequence, including each model initialization (peak values) and the following iterations. From left to right and from top to bottom: approaches 1, 2, 3, 4.

, generate comparable errors along the sequence (the third one gives slightly better results but requires much more parameters). Figure 10 represents the evolution of the error shown in figure 9, but with all intermediate iterations. Remark that the error curves of method 4 in figure 9 is the most regular. Moreover, we can notice that method 4 requires the inversion of a linear system of the form $\boldsymbol{X} = \boldsymbol{BP}$ (by computing the pseudoinverse of the matrix with the SVD) only once, and is therefore much faster than the others.

For all these reasons, we selected method 4 in the next section to compute the quantitative volumetric parameters characterizing the deformation of the left ventricle.

4.2   Experimental results on cardiac images

We present in this section results of the tracking algorithm on the cardiac images described in section 3.

Figure 11 shows the dynamic SPECT sequence on a particular cross-section, with the segmented and reconstructed surfaces superimposed (see section 3.3). It also shows the reconstruction of these two surfaces using either one or two models as explained in section 2.2.4. Figure 12 depicts the same results for the 3D rendering of the surface.

Figure 13 shows the dynamic DSR sequence on a cross-section, first the original image, then the segmented endocardium surface superimposed (see section 3.3), and also the reconstruction of this surface with the parametric model. Figure 14 depicts the same result for the 3D rendering of the surface for three time steps of the sequence.

	FFD	Model	Iterations	Frames	Computation time
SPECT	125	2500	10	8	25
DSR	125	5000	10	18	72

Table 3: Computation times (in minutes) for tracking the complete DSR and SPECT$_2$ sequences (also number of iterations, number of points on the FFD and the models, and number of time frames).

We see from these figures that the method provides an accurate tracking of the myocardium walls, on two different imaging modalities, confirming visually the quantitative results obtained on the previous synthetic data. Table 3 shows the CPU time for each complete time sequence (on a
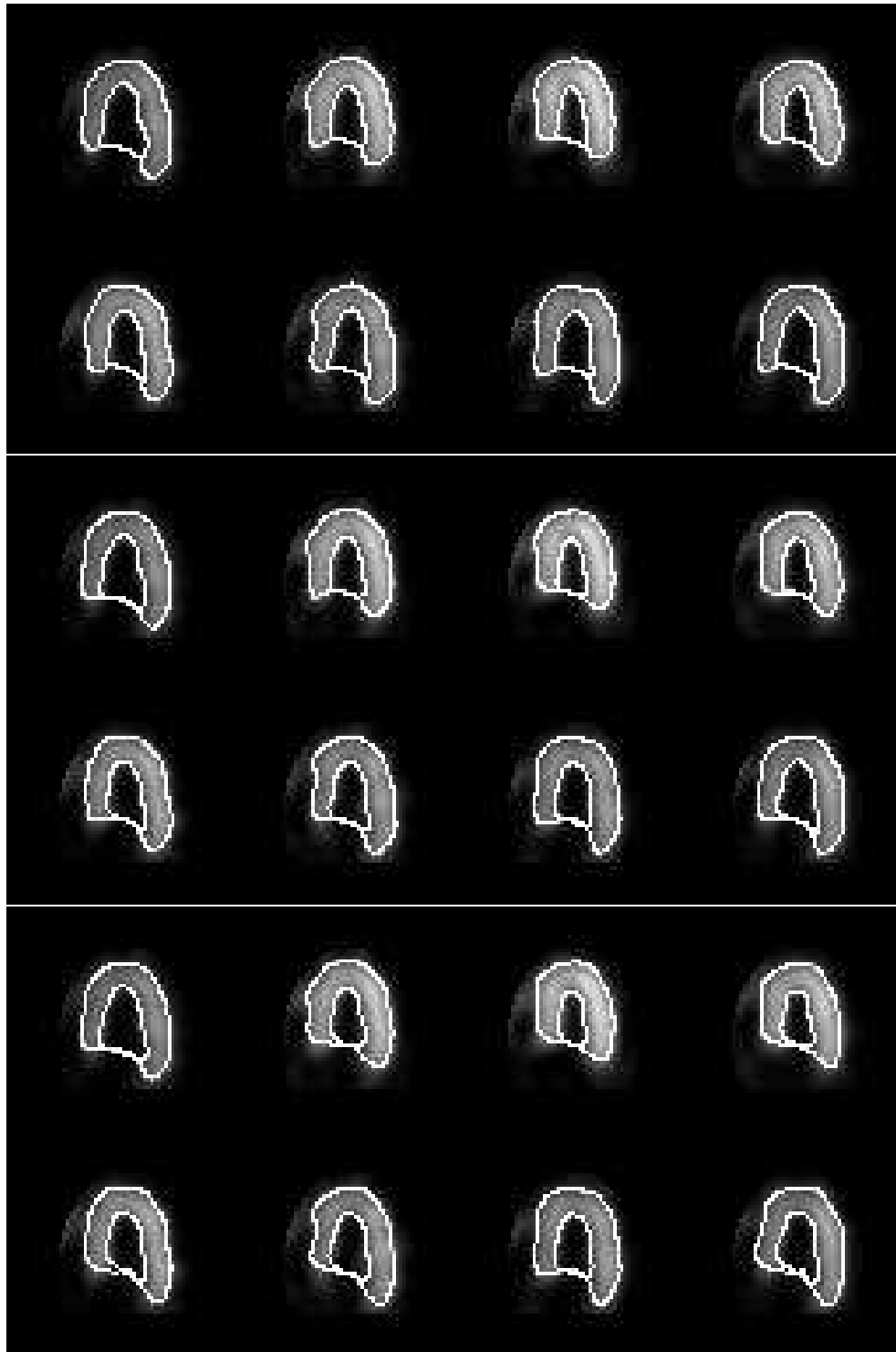
Figure 11: Segmentation and representation of the epicardium and the endocardium (external and internal walls of the ventricle) for a time sequence (3D+T) of the left ventricle during the cardiac cycle - SPECT image; visualization of a cross-section over time. Top: isosurfaces superimposed on the image. Middle: reconstruction of the two isosurfaces by two models. Bottom: simultaneous reconstruction of the two surfaces by one model (see Section 3.3 for details).
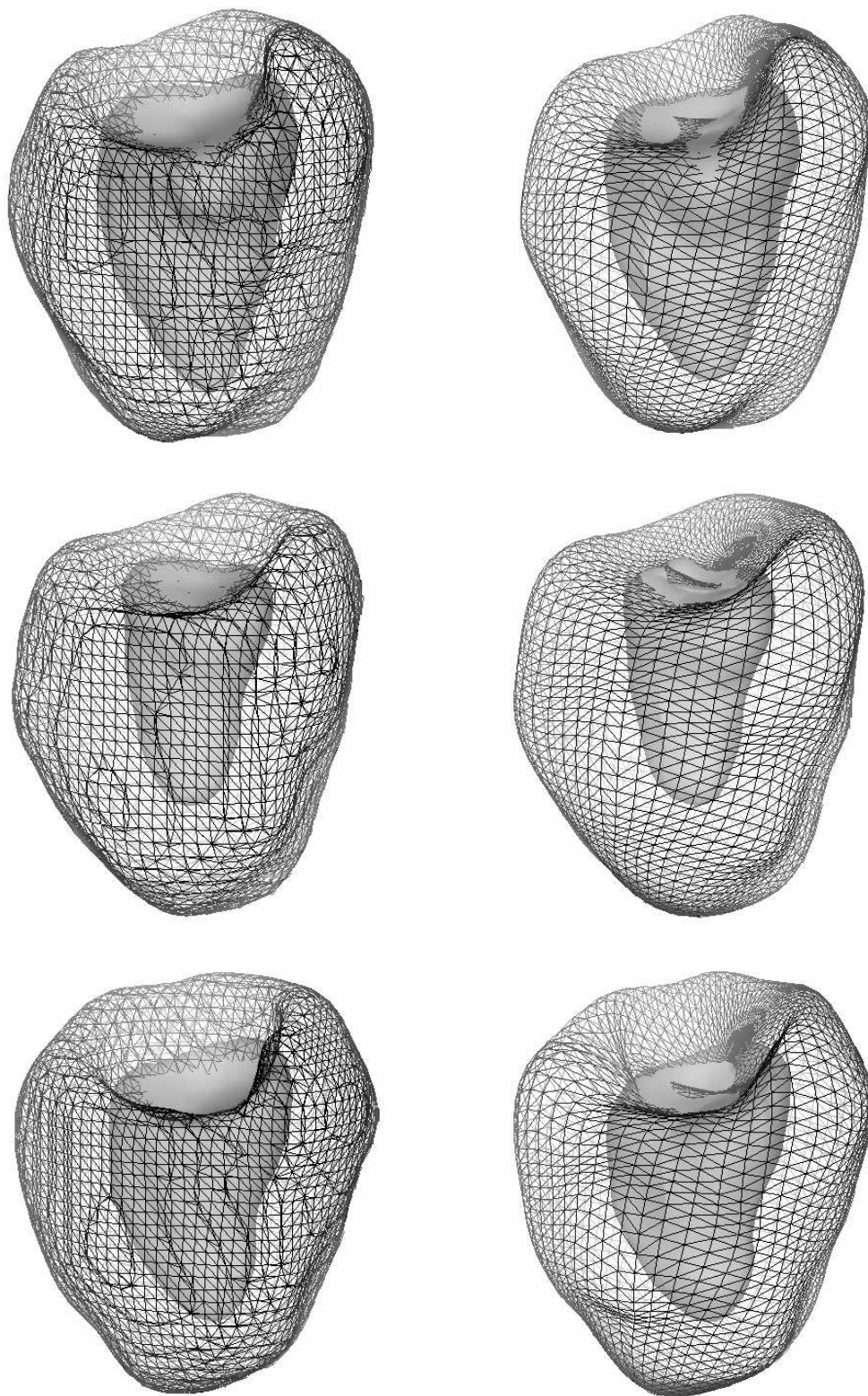
Figure 12: Time sequence of the epicardium (mesh) and the endocardium (rendered surface) - SPECT image. On the left : isosurfaces obtained by data segmentation (4500 + 1500 points). On the right : representation by two parametric models (2×130 parameters).
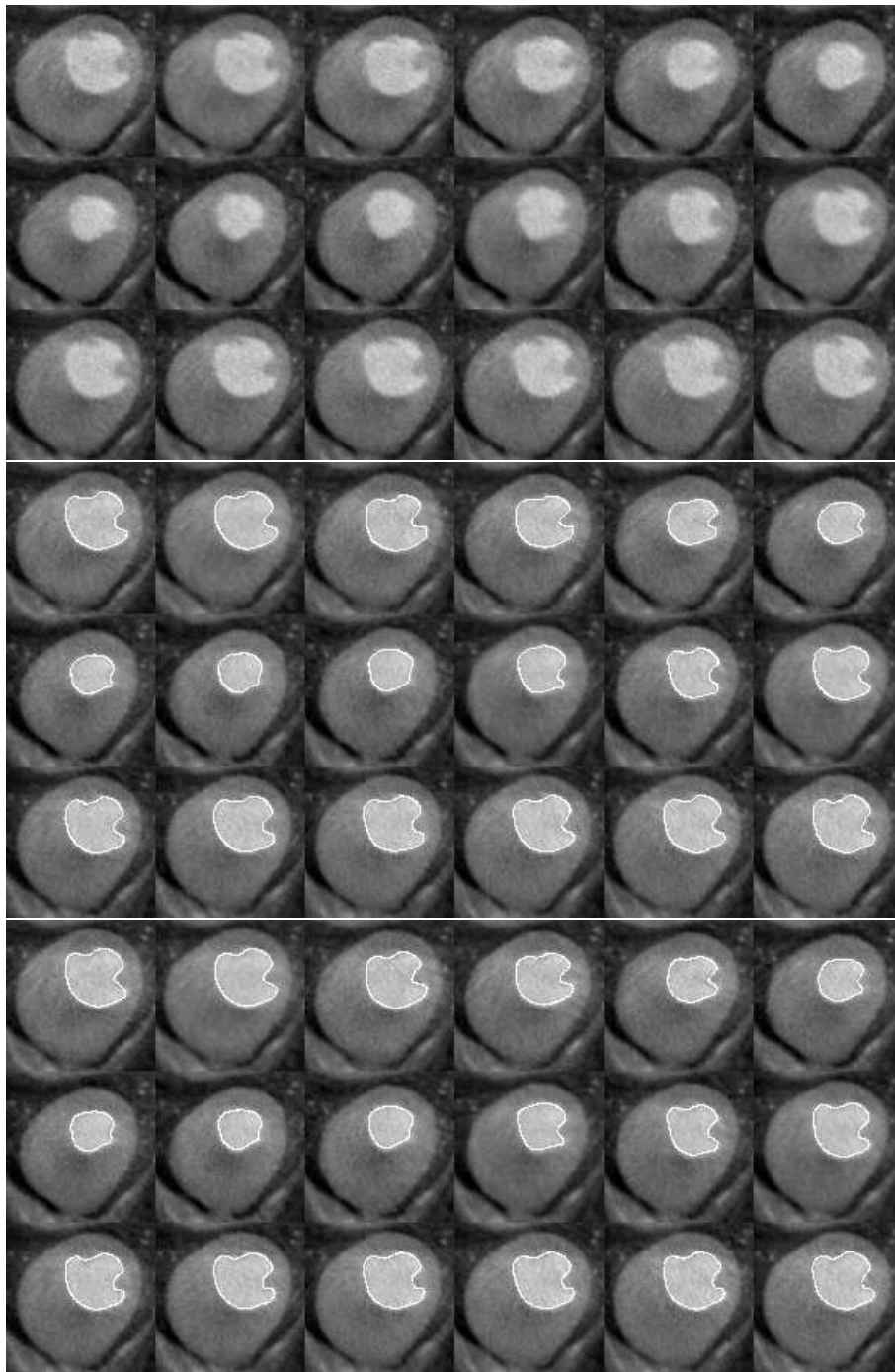
Figure 13: A cross-section over time, during a cardiac cycle (DSR). Top: original image. Middle: segmentation (see section 3.3 for details). Bottom: reconstruction.
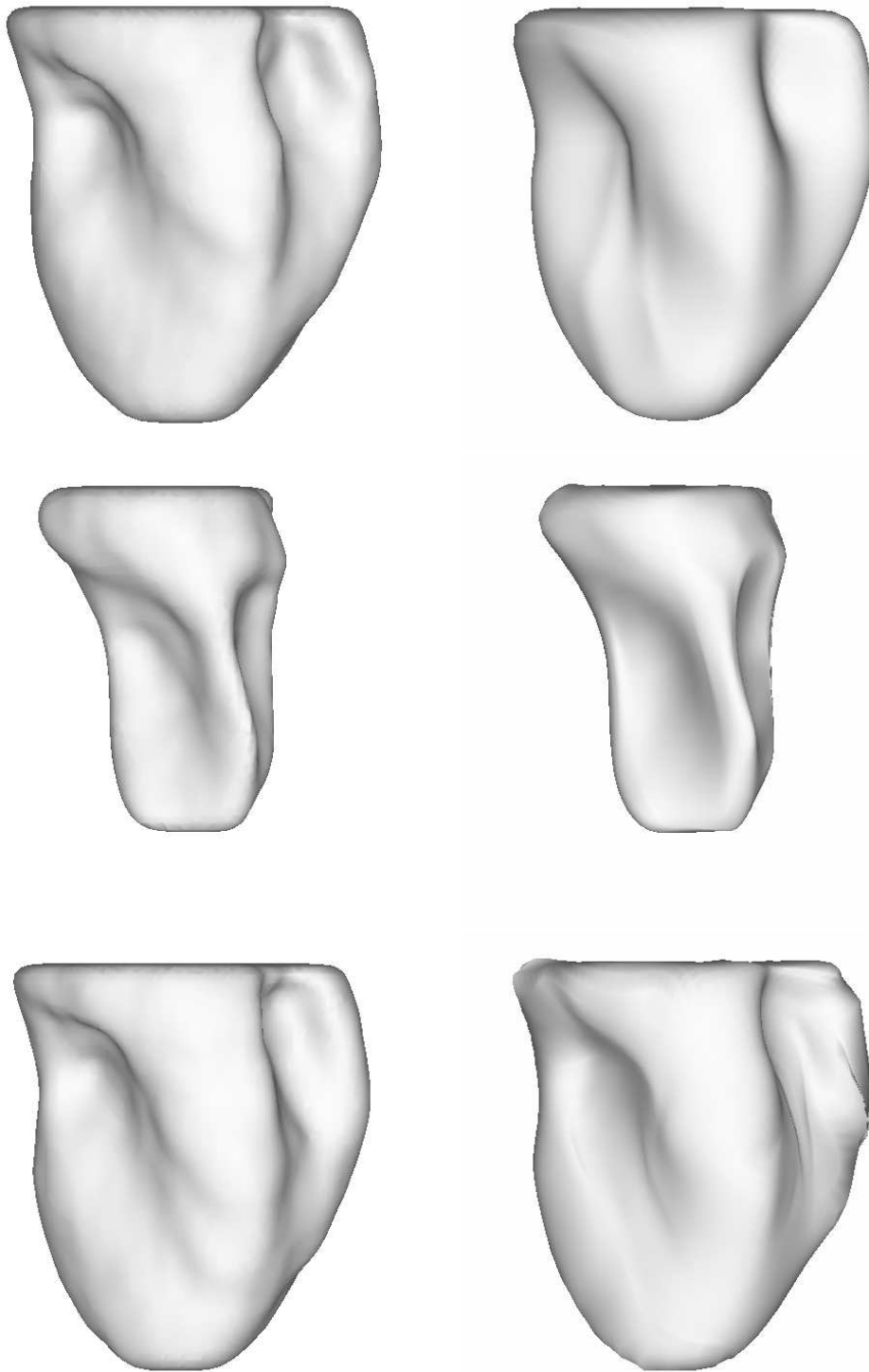
Figure 14: Time sequence of the endocardium (t= 1, 8, 13). On the left : isosurfaces obtained by data segmentation defined by 10000 points. On the right : reconstruction by the parametric model defined by 130 points (DSR). Compression ratio: 77.

DEC Alpha 300).

5   Quantitative analysis of left ventricle deformation

The reconstruction and representation of a time sequence of surfaces by a sequence of parametric models allows to visualize the estimation of the deformation in time. More precisely, the parametric representation provides a way to determine the motion field on the cardiac walls. This motion field can then be used to extract some characteristic parameters and give interpretation or diagnosis on the patient. In the area of cardio-vascular diseases, and especially in the study of cardiac muscle, the useful parameters for diagnosis, as mentioned in the introduction, are primarily the variation of the volume and heart wall thickness during a cardiac cycle, the ejection fraction , and the twist component in the deformation of the ventricle. We explain in this section how we extract those parameters from the previously described parametric representation of time sequences of cardiac images. Similar parameters are also obtained in the work of [30] quantifying the left ventricle deformation.
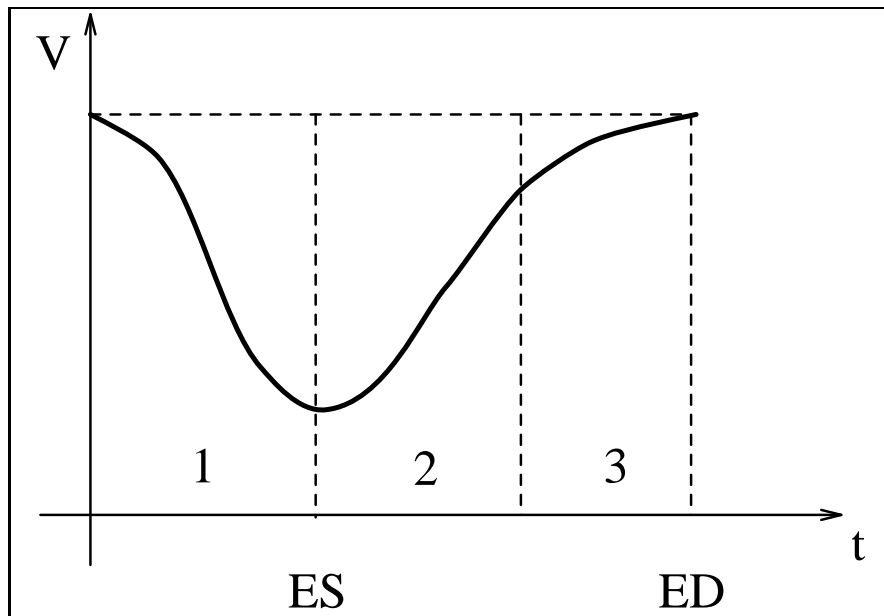
5.1   Volume evolution

Figure 15: Typical shape of the temporal evolution of ventricular volume. The curve is divided into 3 parts: 1. Fast contraction 2. Fast dilation 3. Slow dilation

To evaluate the ejection fraction, we need a way to compute the temporal evolution of the ventricle cavity volume. We first show how to calculate the volume of a polyedric region bounded by a mesh of vertices, using the discrete form of the Gauss integral theorem, and then calculate an explicit form of the volume of a superellipsoid, depending on its parameters.

5.1.1   Volume inside a mesh

Let D be a region of space with bounding surface ∂D; the unit normal vector n to ∂D is drawn outwards. Then:

$$\iiint_D \frac{\partial u(x,y,z)}{\partial x} dx\, dy\, dz = \iint_{\partial D} u \cos(n,x)\, dS \tag{5}$$

(and similarly for y and z). Equation 5 holds under very general assumptions: u must be continuous in D and have continuous bounded first partial derivatives; the boundary surface ∂D must have continuously varying tangent planes, except at finitely many vertices and edges. From this equation, we obtain (among others) the following formula:

$$\iiint_D \boldsymbol{div}\, u = \iint_{\partial D} u\, \boldsymbol{dS} = \iint_{\partial D} (u,n)\, dS \ ,$$

known as the Gauss integral theorem, where $\boldsymbol{div}(.)$ denotes the divergence of a vector field and $(.,.)$ denotes the scalar product in $\mathbb{R}^3$.

Let O be a reference point. Using this theorem, we can write:

$$\iiint_D \boldsymbol{div}(OM)\, dx\, dy\, dz = \iint_{\partial D} (OM, n)\, dS,$$

where M is a point on ∂D. Now, it is obvious that the value of the divergence of the vector field OM is 3. Therefore, the Gauss integral thereom yields an expression of the volume inside a domain D:

$$V = \iiint_D dV = \frac{1}{3} \iint_{\partial D} (OM, n)\, dS \tag{6}$$

Considering an oriented mesh defined by a set of points and a set of facets, the volume inside the mesh can be written, using the previous formula:

$$V = \sum_{i=1}^{K} V_i = \frac{1}{3} \sum_{i=1}^{K} (OM, N)\, S_i, \tag{7}$$

where K is the number of facets of the mesh.

This expression can be rewritten:

$$V = \frac{1}{6} \sum_{i=1}^{K} (OG, N_d) \ ,$$

where N_d and G denote respectively the normal vector and the barycentre of a facet (see appendix A for details of computation).

We applied this calculation of epicardium and endocardium volumes to the sequences of both data points and parametric models obtained in the previous sections. Once we have the values of the volume along a cardiac cycle, we can easily obtain the ejection fraction (calculated precisely as: $\dfrac{Vd - Vc}{Vd}$, with Vd volume at dilation (the end of diastole), Vc volume at contraction (the end of systole), see for example [20]. The results presented in figure 16 show that:

- The evolution of the volume has the expected typical shape found in the medical literature [22] and shown in figure 15. Moreover, the estimation of the ejection fraction on our example gives a value of 68%, which is in the range of expected values [22, 20].

- The volumes computed with all the data points or the approximation models are almost equal as seen from the error curve in figure 16. The relative average error along the cycle is 0.42%. This proves that our model is robust with respect to the volume estimation. Of course, the ejection fraction is also obtained with a very small relative error (0.19%).

- The volume evolution found for initial superellipsoid models before FFD, have also a very similar shape, as seen in figure 16. However, there is a size ratio due to the over-estimation of the volume before the FFD. This ratio is almost constant in time, which makes it possible to get a good estimate of the ejection fraction directly from the initial model. This proves that the superellipsoid model provides a good global estimate of the shape. Also, the volume of the superellipsoid can be obtained analytically from its set of parameters without the previous discrete approximation (see 5.1.2).

5.1.2 Volume of a superellipsoid

Let S be a superellipsoid surface defined by the following implicit equation:

$$\left(\left(\frac{x}{a_1}\right)^{\frac{2}{\epsilon_2}} + \left(\frac{y}{a_2}\right)^{\frac{2}{\epsilon_2}} \right)^{\frac{\epsilon_2}{\epsilon_1}} + \left(\frac{z}{a_3}\right)^{\frac{2}{\epsilon_1}} = 1. \tag{8}$$

Its volume can be explicitly computed by using the following formula:

$$V = 2\, a_1\, a_2\, a_3\, \epsilon_1\, \epsilon_2 \beta\!\left(\frac{\epsilon_2}{2},\, \frac{\epsilon_2}{2} + 1\right) \beta\!\left(\frac{\epsilon_1}{2},\, \epsilon_1 + 1\right)$$
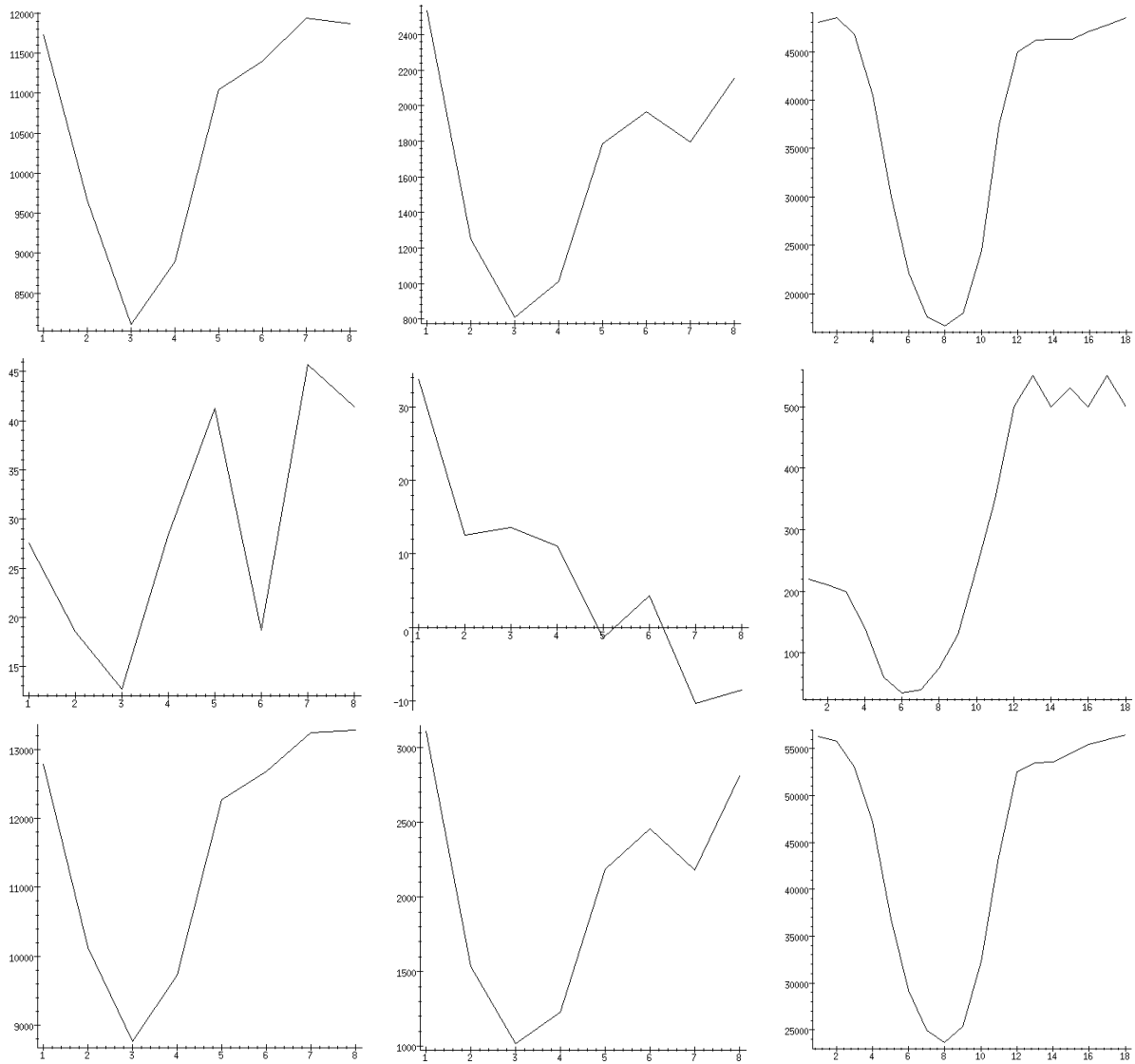
See appendix B for details of computation.

Figure 16: Cardiac volumes during the cardiac cycle. Left: volumes of the epicardium (SPECT). Middle: volumes of the endocardium (SPECT). Right: volumes of the endocardium (DSR). Top: volumes of the data. Middle: errors between the volumes of the data and the volumes of the models. Bottom: volumes of the superellipsoid models. Note that the relative average errors along the cycle are less than 1%.
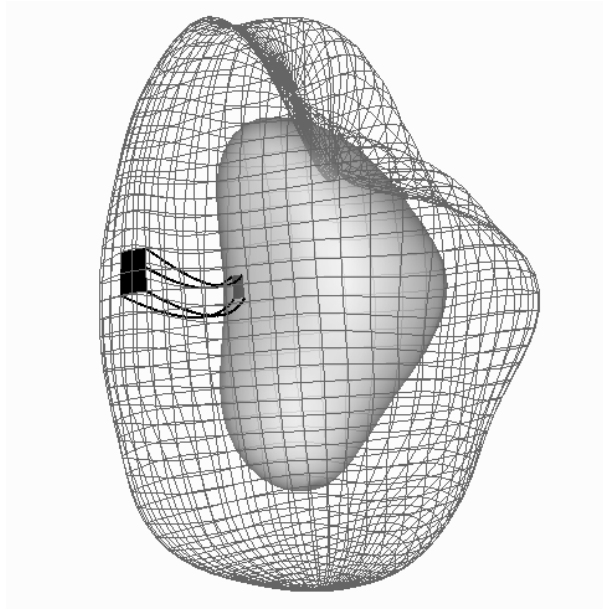
5.2   Wall thickness

Figure 17: One volume element in the volumetric model of the myocardium.

Another important feature that is useful for the diagnosis is the evolution of the wall thickness during the cardiac contraction. Computing only one model to recover the deformation of both the epicardium and the endocardium permits easy calculation of this parameter. Figure 17 represents the volumetric model of the myocardium and a particular volume element. This element is defined by two corresponding rectangular elements on each of the two parameterized surfaces (epicardium and endocardium). The nodes of these rectangles are linked by curvilinear segments that show the volumetric effect of the FFD (see Section 2.2.4). Figure 18 shows the evolution of the wall thickness over time for this given volume element. This thickness has been computed as the difference of the ρ parameters (one of the cylindrical coordinates, see figure 21) for two parametric points on the epicardium and the endocardium. Figure 19 represents the volumetric deformation of the volume element inside the myocardium muscle.

5.3   Trajectories

Listing the successive positions of a parametric point of the deformed surface model along the time sequence, we obtain the trajectory followed by this point. We assume here that the position of a point in the next frame is the closest point to the current data. This hypothesis is valid in the case
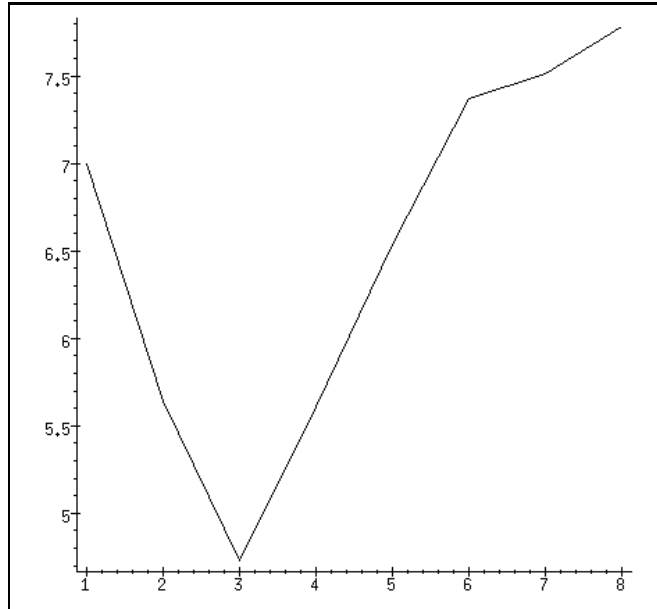
Figure 18: Evolution of the wall thickness during the cardiac cycle for one point of the volumetric model (x axis: time ; y axis: wall thickness).

of small deformations, which means that the time step is not too large. We also assume that the deformation of a point in the parameterization of the surface corresponds to the deformation of the material point of the tissue. Of course, some other constraints could be added to get a better correspondence between the two physical surfaces. In [12, 8, 13, 21], local geometrical properties based on curvature are used to improve the matching between two curves, surfaces or images in a context of registration. However, since the deformation is nonrigid, the differential constraints are not always very significant. We first study in section 5.3.1 an artificial case, where the data consist in the synthetic sequence previously tracked (see section 4.1) on which a twist has been added. Then, we present in section 5.3.2 the trajectories that we computed from the previous cardiac sequences, DSR and SPECT.

5.3.1 Synthetic example

Starting from the synthetic sequence that we previously tracked, we added a twist (from $-\alpha$ on the apex to $+\alpha$ on the base, with α varying from 0° up to 30°, then back to 0°) on this sequence and tried to recover the a priori known trajectories using the four tracking strategies. Recovering a twist motion is a difficult problem, since the displacement of each point has a tangential component
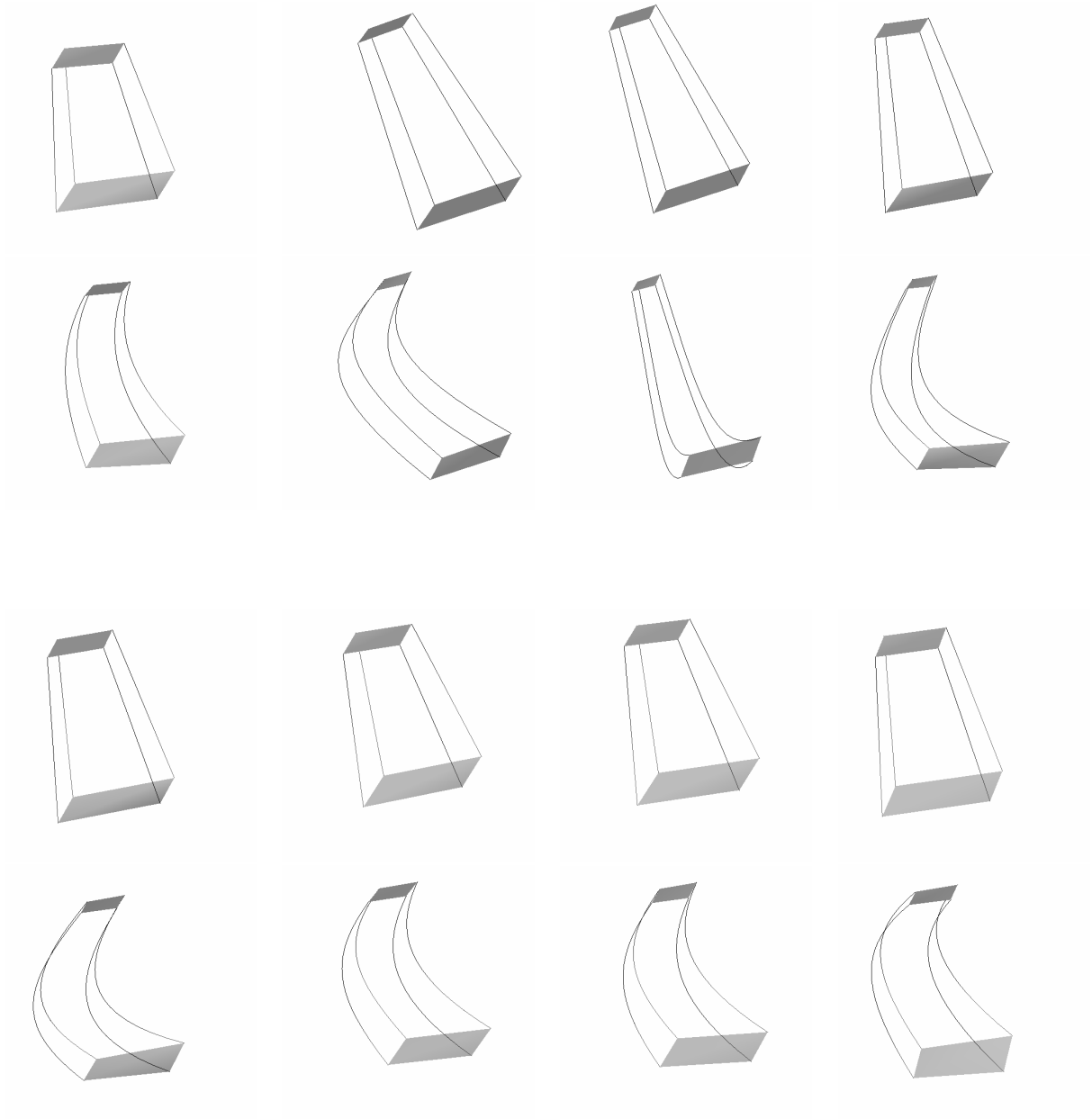
Figure 19: Deformation of a volume element inside the myocardium during the cardiac cycle (8 time steps). Rows 1 and 3: volume element between the superellipsoid models. Rows 2 and 4: volume element between the final models, after the volumetric deformation.

which cannot be easily detected. Figure 20 presents the trajectories found with the four strategies compared to the original ones. One can see that the two temporal tracking methods (3 and 4) provide results which are close to the original trajectories, and catch the twist component of the motion, contrary to methods 1 and 2. Remark also that trajectories found with method 4 seem smoother than the ones found with method 3. This is due to the use of only one FFD to recover all the sequence.

To quantify the twist component of the motion, once the trajectories have been computed, we decompose the corresponding displacement vectors in cylindrical coordinates (see figure 21):

$$
\begin{pmatrix} x \\ y \\ z \end{pmatrix} \rightarrow \begin{pmatrix} \rho & = & \sqrt{x^2 + y^2} \\ \theta & = & arcos\left(\dfrac{x}{\sqrt{x^2 + y^2}}\right) \\ z & = & z \end{pmatrix} \tag{9}
$$

The z-axis for the cylindrical representation correspond to the z-axis of inertia of the superellipsoid model. To measure the twist, we compute the difference of the θ parameters for the two points that represent the same parametric point during the contraction. Figure 22 represents the ranges of this twist, on the original synthetic data and for the models recovered by each of the four tracking methods. Remark again that the twist component is pretty well recovered with the temporal tracking methods (3 and 4). The maximum value of α on the models is 27° for method 3 and 26° for method 4 (to be compared with 30°).

5.3.2 Experimental results

Figures 23 and 24 show the trajectories of the node points between the end of diastole and the end of systole for the DSR and SPECT data. These are visualized from different viewpoints to better appreciate the motion. One can see, especially from the upper and lower viewpoints on figure 24, that our tracking methods catch the characteristic twist component of the motion. Figure 25 represents the mean values of $\theta' - \theta$ (in radians) along the different latitudes. One can see that the twist is in the range 10 - 12 degrees which is the expected range.

The pointwise tracking of the deformation allows an evaluation of the velocity field during the sequence. The visualization of these displacements by different values, according to their range, on the surface shows up clearly areas on the ventricle where the deformation is weak (see figure 26). This visualization could be used by the physician to help localize pathologies like infarcted regions.
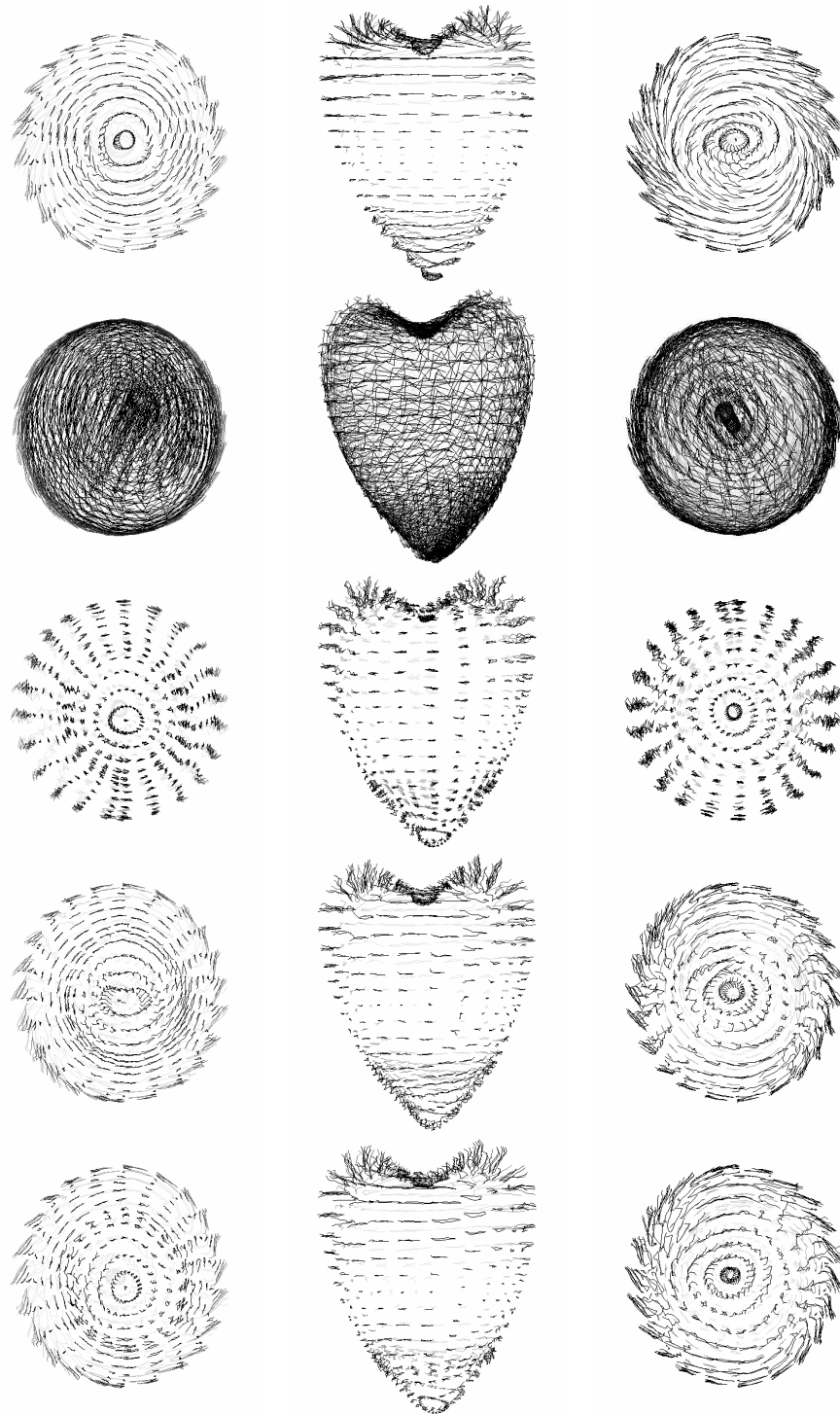
Figure 20: Trajectories on a synthetic example. Top: original trajectories. Bottom: trajectories computed with strategies 1, 2, 3 and 4. Left column: view from the apex. Middle column: front view. Right column: view from the base.
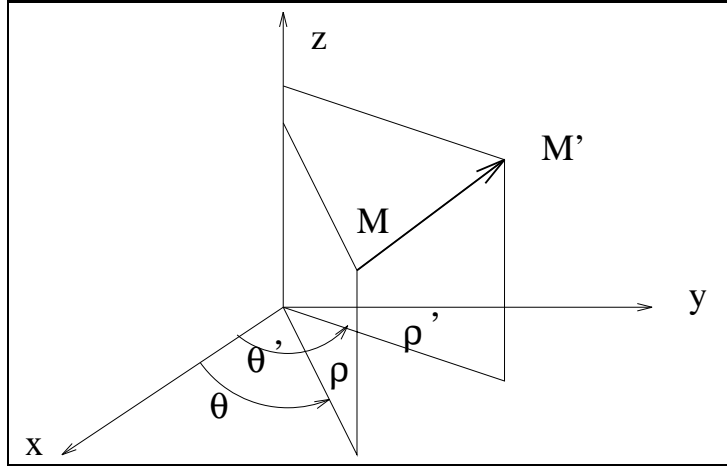
Figure 21: Cylindrical coordinates of two points M and M', which represent the same parametric point at the beginning and at the end of the cardiac cycle.

6   Conclusion

We presented a new approach to analyze the deformation of the heart left ventricle with a parametric model. It is based on a parametric model that gives a compact representation of a set of points in a 3-D image. We presented four approaches using this model to track efficiently the left ventricle walls in a sequence of 3D images during a cardiac cycle and compared on synthetic and real data. The model is able to track simultaneously the endocardium and the epicardium walls, since it is a volumetric deformation. Experimental results have been shown for automatic shape tracking in a time sequence of cardiac images.

The reconstruction and representation of a time sequence of surfaces by a sequence of parametric models has then allowed to infer some characteristic parameters useful to the physician, such as the variation of the volume and heart wall thickness during a cardiac cycle, the ejection fraction and the twist component in the deformation of the ventricle.

In some cases, the tracking can be helped by adding hard constraints when there is *a priori* knowledge of the deformation at some reliable anchor points. This is the case in tagged images, where some tissues are marked and can be tracked after a simple preprocessing [2, 24, 44, 30, 27]. We hope to apply our work to this recent technique of imaging in a the near future.
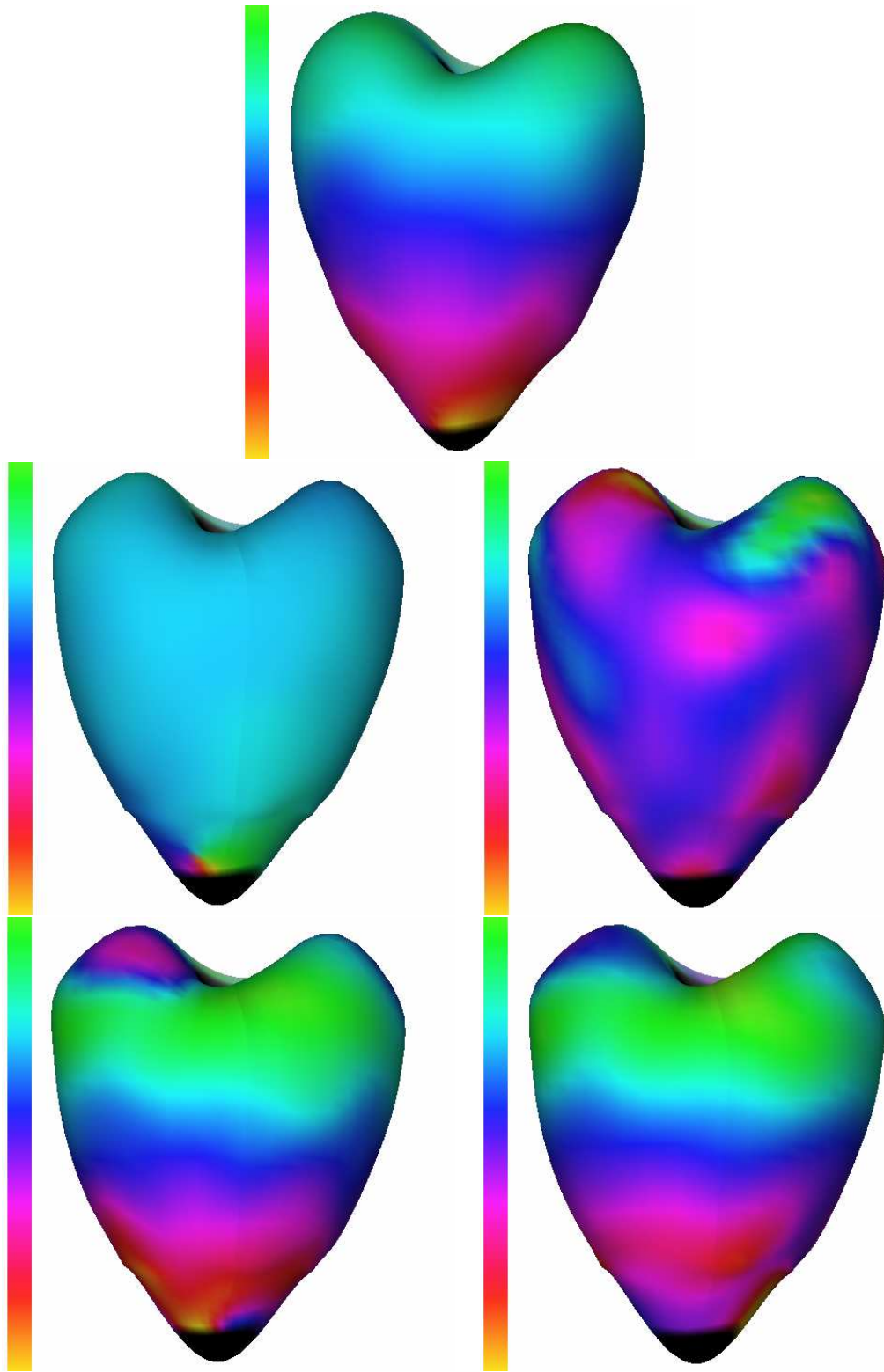
Figure 22: Twist component estimation on a synthetic example. Top: from original data. From left to right and from top to bottom: from models obtained using strategies 1, 2, 3 and 4.
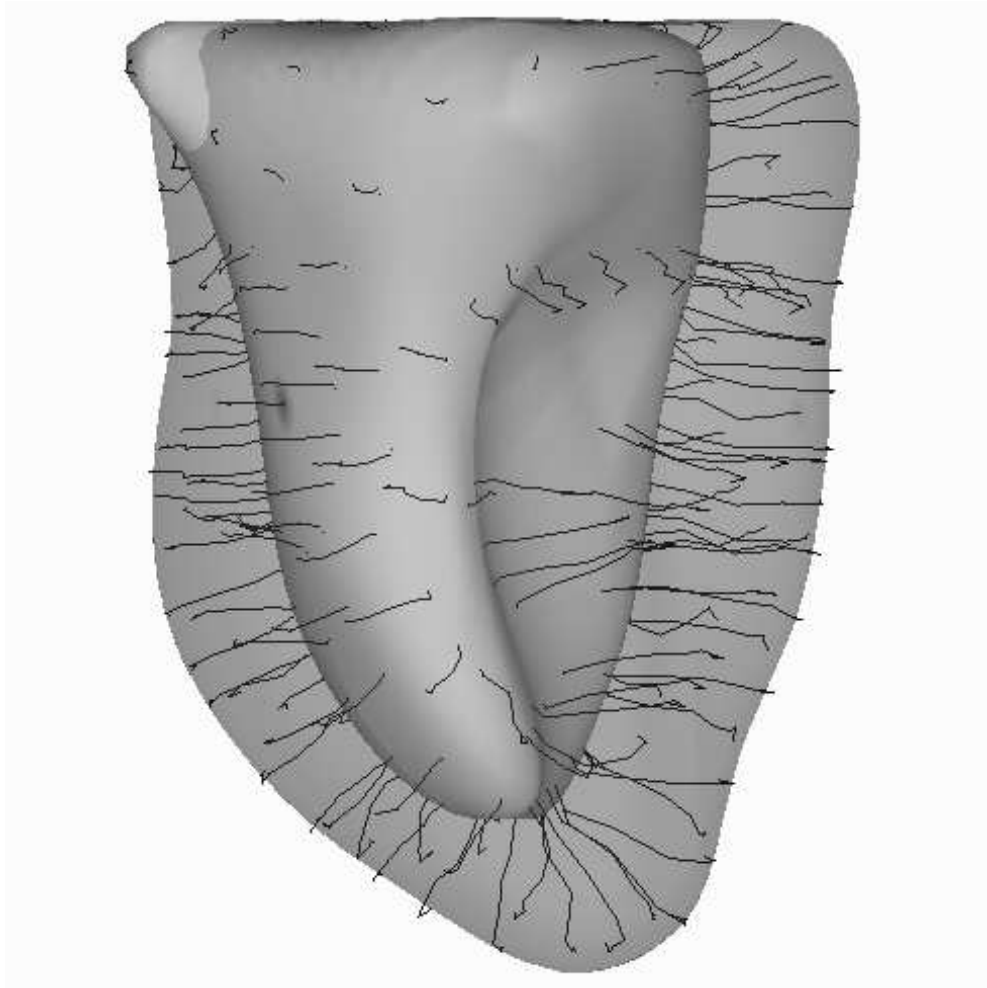
Figure 23: Trajectories of points on the model of the endocardium during a cardiac cycle (DSR). The two surfaces represent the models at end of diastole (dilation) and end of systole (contraction).
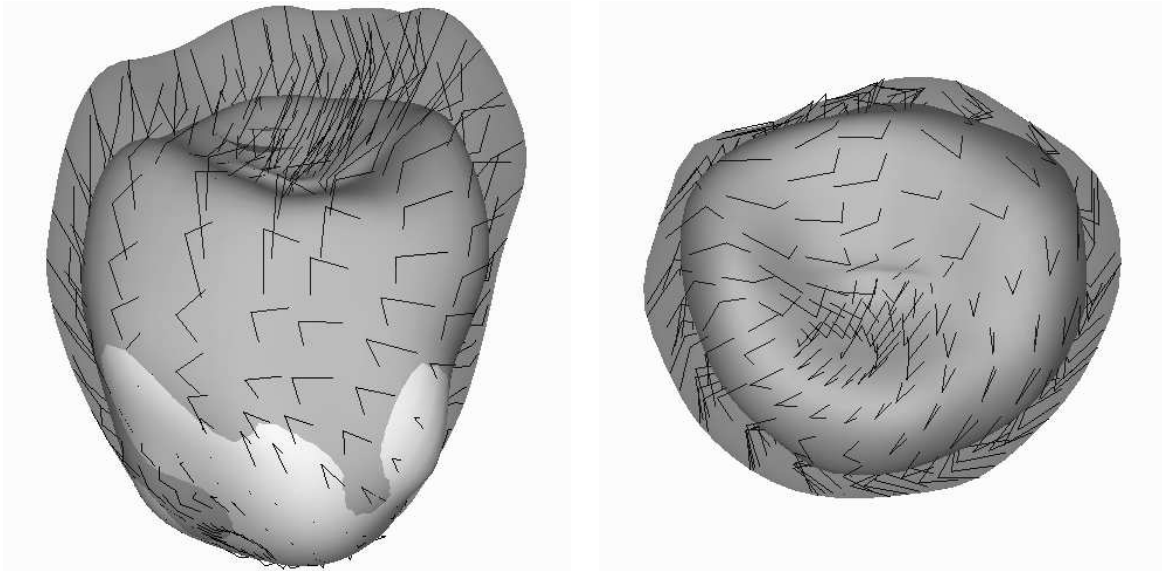
Figure 24: Trajectories of points on the model of the epicardium during a cardiac cycle from 2 viewpoints (SPECT). The two surfaces represent the models at end of diastole (dilation) and end of systole (contraction).
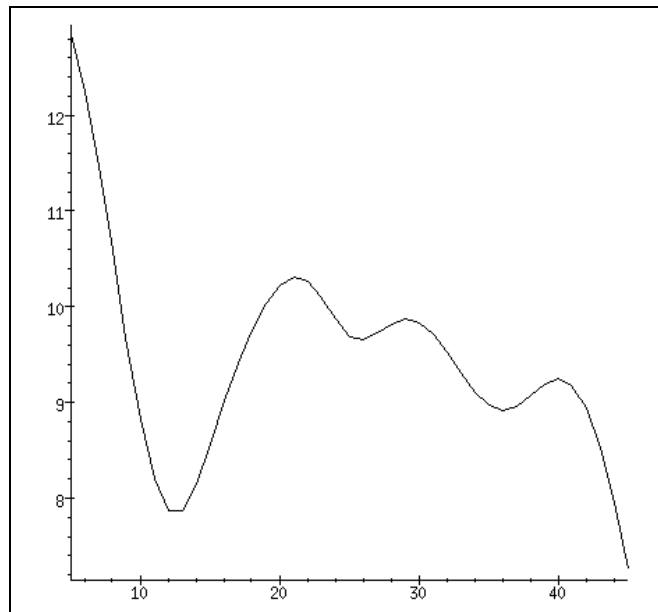

Figure 25: Profile of the mean twist during the cardiac cycle along the z-axis (0 and 50 on the x axis correspond to the positions of the two poles in the parameterization).
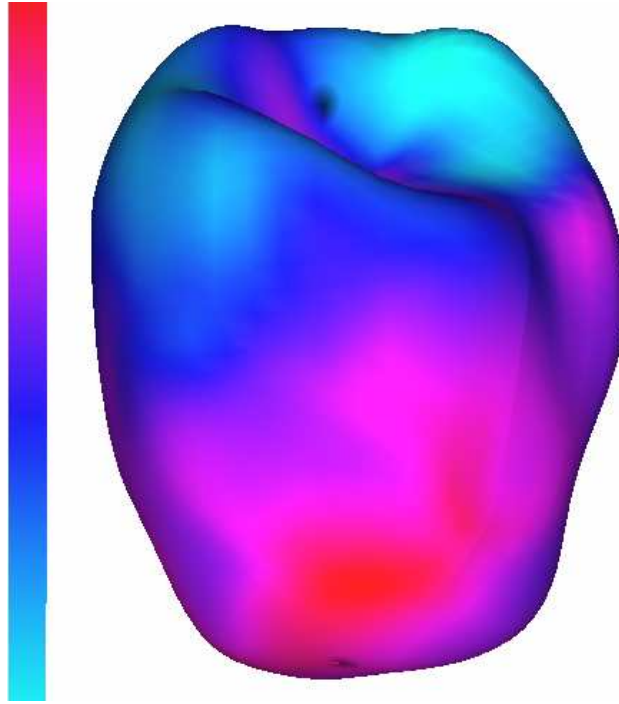
Figure 26: Range of the displacements of the points on the model during a cardiac cycle.

Acknowledgements

A   Calculation of the volume inside a mesh

From equations (6) and (7), considering an oriented mesh defined by a set of points and a set of facets, the volume inside the mesh can be written:

$$V = \frac{1}{3} \sum_{i=1}^{K} (OM, N) \, S_i, \tag{10}$$

where K is the number of facets of the mesh.

We have to define the normal vector of a facet. Assuming that the facet is defined by 3 points A_1, A_2 and A_3, the normal vector can be written:

$$N_d = (A_1 - A_2) \wedge (A_1 - A_3) = A_1 \wedge A_2 + A_2 \wedge A_3 + A_3 \wedge A_1,$$

where $(. \wedge .)$ denotes the vector product. Note that the norm of this normal vector is linked to the surface S of the facet as follows: $\| N_d \| = 2S$. One can easily generalize this formula for a facet defined by a set of points A_i, $i = 1..M$:

$$N_d = \sum_{i=1}^{M-1} (A_i \wedge A_{i+1}) + A_M \wedge A_1$$

This expression can be seen as the average of the normal vectors of the decomposition of the facet into triangular sub-facets.

Let suppose that the mesh is composed of triangular facets defined by A_1, A_2 and A_3. The volume V_i of the tetrahedron $OA_1A_2A_3$ is:

$$V_i = \frac{S.H}{3},$$

where H is the height. Let O be the origin and G be the barycentre of a facet. Then:

$$H = \frac{(OG, N_d)}{\| N_d \|}$$

And therefore:

$$V_i = \frac{(OG, N_d)}{6}$$

This last expression is still true for a facet defined by M points. Finally, equation 10 can be rewritten:

$$V = \frac{1}{6} \sum_{i=1}^{K} (OG, N_d)$$

B   Calcultion of the volume of a superellipsoid

Let S be a superellipsoid surface defined by the following implicit equation:

$$\left(\left(\frac{x}{a_1} \right)^{\frac{2}{\epsilon_2}} + \left(\frac{y}{a_2} \right)^{\frac{2}{\epsilon_2}} \right)^{\frac{\epsilon_2}{\epsilon_1}} + \left(\frac{z}{a_3} \right)^{\frac{2}{\epsilon_1}} = 1. \tag{11}$$

An explicit parameterization of S is given by:

$$\begin{cases} x &=& a_1 \cos^{\epsilon_1} \eta \, \cos^{\epsilon_2} \omega \\ y &=& a_2 \cos^{\epsilon_1} \eta \, \sin^{\epsilon_2} \omega \\ z &=& a_3 \sin^{\epsilon_1} \eta \end{cases} \quad , \quad \begin{array}{c} -\frac{\pi}{2} \leq \eta \leq \frac{\pi}{2} \\ -\pi \leq \omega < \pi \end{array}$$

Due to the symmetry of the surface in relation to the 3 axes of the coordinate system, the computation of the volume inside S can be made as follows:

$$V = 2 \int_0^{a_3} A(z) \, dz, \tag{12}$$

where $A(z)$ is the area of a slice among the z-axis. For $\eta = 0$, the implicit equation of the corresponding slice is:

$$\left(\frac{x}{a_1}\right)^{\frac{2}{\epsilon_2}} + \left(\frac{y}{a_2}\right)^{\frac{2}{\epsilon_2}} = 1$$

This leads to:

$$A(0) = 4 \, a_2 \int_0^{a_1} y(x) \, dx = 4 \, a_2 \int_0^{a_1} \left[1 - \left(\frac{x}{a_1}\right)^{\frac{2}{\epsilon_2}}\right]^{\frac{\epsilon_2}{2}} dx$$

Setting: $X = \left(\frac{x}{a_2}\right)^{\frac{\epsilon_2}{2}}$, it becomes:

$$A(0) = 2 \, a_1 \, a_2 \, \epsilon_2 \, \beta\left(\frac{\epsilon_2}{2}, \frac{\epsilon_2}{2} + 1\right),$$

where $\beta(x, y)$ denotes the Beta function (Euler's integral of the first kind):

$$\beta(x, y) = \int_0^1 t^{x-1}(1 - t)^{y-1} \, dt$$

Finally, to calculate the volume inside S using equation 12, we have to write a_1 and a_2 as functions of z. From the implicit definition of S (Equation 11), we deduce:

$$a_1(z) = a_1\left[1 - \left(\frac{z}{a_3}\right)^{\frac{2}{\epsilon_1}}\right]^{\frac{\epsilon_1}{2}} \quad , \quad a_2(z) = a_2\left[1 - \left(\frac{z}{a_3}\right)^{\frac{2}{\epsilon_1}}\right]^{\frac{\epsilon_1}{2}}$$

Therefore:

$$V = 2 \int_0^{a_3} 2 \, \epsilon_2 \, \beta\left(\frac{\epsilon_2}{2}, \frac{\epsilon_2}{2} + 1\right) a_1(z) \, a_2(z) \, dz$$

Setting: $Z = \left(\frac{z}{a_3}\right)^{\frac{2}{\epsilon_1}}$, it becomes:

$$V = 2 \, a_1 \, a_2 \, a_3 \, \epsilon_1 \, \epsilon_2 \beta\left(\frac{\epsilon_2}{2}, \frac{\epsilon_2}{2} + 1\right) \beta\left(\frac{\epsilon_1}{2}, \epsilon_1 + 1\right)$$

Note that for a sphere ($\epsilon_1 = \epsilon_2 = 1$, $a_1 = a_2 = a_3 = R$), the previous formula gives:

$$V = 2 \, R^3 \, B\left(\frac{1}{2}, \frac{3}{2}\right) B\left(\frac{1}{2}, 2\right) = \frac{4}{3} \pi \, R^3$$

Content of the video

The video consists in 6 sequences:

1. Nuclear medicine data (SPECT image). The first image of the sequence is visualized as a series of 2D cross-sections (transverse slices). See section 3 for details.

2. Segmentation of the SPECT sequence. See section 3 for details.

3. Tracking of the epicardium (mesh) and the endocardium (rendered surface) in the SPECT sequence; on the left, the segmented surfaces, on the right, the reconstructed models. See sections 3 and 4.2 for details.

4. On the left, trajectories of the node points, on the right, velocity field during the SPECT sequence. See section 5.3.2 for details.

5. Recovery of a twist motion on a synthetic example (1). Data with trajectories. See section 5.3.1 for details.

6. Recovery of a twist motion on a synthetic example (2). Trajectories on the data and on the models computed with tracking method 4. See section 5.3.1 for details.

References

[1] R. Acharya, R. Wasserman, J. Stevens, and C. Hinojosa. Biomedical imaging modalities: a tutorial. *Computerized Medical Imaging and Graphics*, 19(1):3–25, 1995.

[2] A. Amini, R. Curwen, R. Constable, and J. Gore. MR physics-based snake tracking and dense deformations from tagged cardiac images. In *AAAI Symposium on Applications of Computer Vision to Medical Image Processing*, pages 126–129, Stanford, California, March 1994.

[3] A. Amini and J. Duncan. Bending and stretching models for LV wall motion analysis from curves and surfaces. *Image and vision computing*, 10:418–430, August 1992.

[4] A. Amini, R. Owen, P. Anandan, and J. Duncan. Non-rigid motion models for tracking the left ventricular wall. In *Information processing in medical images*, Lecture notes in computer science, pages 343–357, 1991. Springer-Verlag.

[5] N. Ayache, J.D. Boissonnat, E. Brunet, L. Cohen, J.P. Chièze, B. Geiger, O. Monga, J.M. Rocchisani, and P. Sander. Building highly structured volume representations in 3D medical images. In *Computer Aided Radiology*, June 1989. Berlin, West-Germany.

[6] N. Ayache, J.D. Boissonnat, L. Cohen, B. Geiger, O. Monga, J. Levy-Vehel, and P. Sander. Steps toward the automatic interpretation of 3D images. *NATO ASI Series on 3D Imaging in Medicine*, F 60:107–120, 1990.

[7] N. Ayache, P. Cinquin, I. Cohen, L. Cohen, F. Leitner, and O. Monga. *Segmentation of complex 3D medical objects : a challenge and a requirement for computer assisted surgery planning and performing.* MIT Press, 1994.

[8] N. Ayache, I. Cohen, and I. Herlin. *Medical Image Tracking*, chapter 20. MIT Press, 1992.

[9] R. Bajcsy and F. Solina. Three dimensional object representation revisited. In *Proceedings IEEE International Conference on Computer Vision (ICCV)*, pages 231–240, London, June 1987.

[10] E. Bardinet, L. Cohen, and N. Ayache. Fitting of iso-surfaces using superquadrics and free-form deformations. In *Proceedings IEEE Workshop on Biomedical Image Analysis (WBIA)*, Seattle, Washington, June 1994.

[11] E. Bardinet, L.D. Cohen, and N. Ayache. Superquadrics and free-form deformations: a global model to fit and track 3D medical data. In *Proceedings Conference on Computer Vision, Virtual Reality and Robotics in Medecine (CVRMed)*, Nice, France, April 1995.

[12] S. Benayoun, N. Ayache, and I. Cohen. Adaptive meshes and nonrigid motion computation. In *Proceedings International Conference on Pattern Recognition (ICPR)*, Jerusalem, Israel, October 1994.

[13] S. Benayoun, C. Nastar, and N. Ayache. Dense non-rigid motion estimation in sequences of 3D images using differential constraints. In *Proceedings Conference on Computer Vision, Virtual Reality and Robotics in Medecine (CVRMed)*, pages 309–318, Nice, France, April 1995.

[14] A. Blake and A. Zisserman. *Visual Reconstruction.* MIT Press, 1987.

[15] I. Cohen and L.D. Cohen. A hybrid hyperquadric model for 2-D and 3-D data fitting. In *Proceedings International Conference on Pattern Recognition (ICPR)*, pages B–403–405, Jerusalem, October 1994. Part of Inria TR 2188, to appear in *Computer Vision, Graphics, and Image Processing : Image Understanding.*

[16] I. Cohen, L.D. Cohen, and N. Ayache. Using deformable surfaces to segment 3-D images and infer differential structures. *Computer Vision, Graphics, and Image Processing: Image Understanding*, 56(2):242–263, September 1992.

[17] L.D. Cohen. On active contour models and balloons. *Computer Vision, Graphics, and Image Processing: Image Understanding*, 53(2):211–218, March 1991. INRIA TR 1075, August 1989.

[18] L.D. Cohen. Auxiliary variables and two-step iterative algorithms in computer vision problems. Technical report, Ceremade, Février 1995. Cahiers de Mathématiques de la Décision 9511, to appear in Journal of Mathematical Imaging and Vision and Proceedings ICCV'95, Boston.

[19] L.D. Cohen and I. Cohen. Finite element methods for active contour models and balloons for 2-D and 3-D images. *IEEE Transactions on Pattern Analysis and Machine Intelligence*, 15(11), November 1993.

[20] M. Davis, B. Rezaie, and F. Weiland. Assessment of left ventricular ejection fraction from technetium-99m-methoxy isobutyl isonitrile multiple-gated radionuclide angiocardoigraphy. *IEEE Transactions on Medical Imaging*, 12(2):189–199, June 1993.

[21] J. Feldmar and N. Ayache. Locally affine registration of free-form surfaces. In *Proceedings IEEE Computer Society Computer Vision and Pattern Recognition (CVPR)*, Seattle, USA, June 1994. To appear in *International Journal of Computer Vision*.

[22] M. Goris and J. Bretille. *A colour atlas of nuclear cardiology*. Chapman and Hall, 1992.

[23] W. E. L. Grimson. *From Images to Surfaces: A computational study of the Human Early vision system*. The MIT Press, 1981.

[24] M.A. Guttman, J.L. Prince, and E.R. McVeigh. Tag and Contour Detection in Tagged MR Images of the Left Ventricle. In *IEEE Transactions on Medical Imaging*, volume 13, pages 74–88, March 1994.

[25] K. Höhne and W. Hanson. Interactive 3D segmentation of MRI and CT volumes using morphological operations. *Journal of Computer Assisted Tomography*, 16(2):285–294, March 1992.

[26] M. Kass, A. Witkin, and D. Terzopoulos. Snakes: active contour models. *International Journal of Computer Vision*, 1:321–331, 1987.

[27] S. Kumar and D. Goldgof. Automatic Tracking of SPAMM Grid and the Estimation of Deformation Parameters from Cardiac MR Images. In *IEEE Transactions on Medical Imaging*, pages 122–132, March 1994.

[28] F. Leitner and P. Cinquin. Dynamic segmentation: Detecting complex topology 3D-object. In *Proceedings International Conference of the IEEE Engineering in Medicine and Biology Society*, pages 295–296, Orlando, Florida, November 1991.

[29] T. McInerney and D. Terzopoulos. A dynamic finite element surface model for segmentation and tracking in multidimensional medical images with application to cardiac 4D image analysis. *Computerized Medical Imaging and Graphics*, 19:69–83, January 1995.

[30] J. Park, D. Metaxas, and A. Young. Deformable models with parameter functions : application to heart-wall modeling. In *Proceedings IEEE Computer Society Computer Vision and Pattern Recognition (CVPR)*, pages 437–442, June 1994.

[31] A. Pentland and B. Horowitz. Recovery of nonrigid motion and structure. *IEEE Transactions on Pattern Analysis and Machine Intelligence*, 13(7):730–742, July 1991.

[32] A.P. Pentland. Recognition by parts. In *Proceedings IEEE International Conference on Computer Vision (ICCV)*, pages 612–620, 1987.

[33] T.W. Sederberg and S.R. Parry. Free-form deformation of solid geometric models. *Computer Graphics (Proceedings SIGGRAPH'86)*, 20(4):151–160, August 1986.

[34] J. Serra. *Image analysis and mathematical morphology*, volume 1. Academic Press, 1982.

[35] J. Serra. *Image analysis and mathematical morphology: theoretical advances*, volume 2. Academic Press, 1988.

[36] P. Shi, A. Amini, G. Robinson, A. Sinusas, C. Constable, and J. Duncan. Shape-based 4D left ventricular myocardial function analysis. In *Proceedings IEEE Workshop on Biomedical Image Analysis (WBIA)*, pages 88–97, Seattle, June 1994.

[37] F. Solina and R. Bajcsy. Range image interpretation of mail pieces with superquadrics. In *AAAI*, pages 733–737, Seattle, 1987.

[38] F. Solina and R. Bajcsy. Recovery of parametric models from range images : The case for superquadrics with global deformations. *IEEE Transactions on Pattern Analysis and Machine Intelligence*, 12(2):131–147, February 1990.

[39] R. Szeliski and S. Lavallée. Matching 3D anatomical surfaces with non-rigid deformations. In *Proceedings SPIE Geometric Methods in Computer Vision II*, volume 2031, pages 306–315, San Diego, July 1993. Society of Photo-Optical Instrumentation Engineers.

[40] R. Szeliski and S. Lavallée. Matching 3-d anatomical surfaces with non-rigid deformations using octree-splines. In *Proceedings IEEE Workshop on Biomedical Image Analysis (WBIA)*, Seattle, Washington, June 1994.

[41] D. Terzopoulos. The computation of visible-surface representations. *IEEE Transactions on Pattern Analysis and Machine Intelligence*, 10(4):417–438, July 1988.

[42] D. Terzopoulos and D. Metaxas. Dynamic 3D models with local and global deformations: deformable superquadrics. *IEEE Transactions on Pattern Analysis and Machine Intelligence*, 13(7):703–714, July 1991.

[43] D. Terzopoulos, A. Witkin, and M. Kass. Symmetry-seeking models for 3D object reconstruction. *International Journal of Computer Vision*, 1(3):211–221, October 1987.

[44] A.A. Young, D.L. Kraitchman, and L. Axel. Deformable Models for Tagged MR Images : Reconstruction of 2- and 3-Dimensional Heart Wall Motion. In *IEEE Workshop on Biomedical Image Analysis*, pages 317–323, June 1994.

[45] A.L. Yuille, P.W. Hallinan, and D.S. Cohen. Feature extraction from faces using deformable templates. *International Journal of Computer Vision*, 8(2):99–111, September 1992.